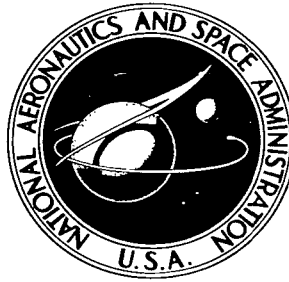


NASA TECHNICAL NOTE



NASA TN D-3276

NASA TN D-3276

LOAN COPY: 7777  
APR 1966  
KIMBERLY

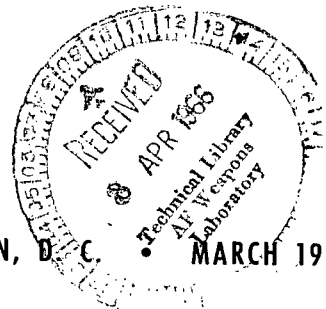
0079794



EFFECT OF GEOMETRIC MODIFICATIONS  
ON THE MAXIMUM LIFT-DRAG RATIOS  
OF SLENDER WING-BODY CONFIGURATIONS  
AT HYPERSONIC SPEEDS

*by William J. Small and Mitchel H. Bertram*

*Langley Research Center  
Langley Station, Hampton, Va.*



NATIONAL AERONAUTICS AND SPACE ADMINISTRATION • WASHINGTON, D. C. • MARCH 1966



EFFECT OF GEOMETRIC MODIFICATIONS ON THE MAXIMUM  
LIFT-DRAG RATIOS OF SLENDER WING-BODY CONFIGURATIONS  
AT HYPERSONIC SPEEDS

By William J. Small and Mitchel H. Bertram

Langley Research Center  
Langley Station, Hampton, Va.

NATIONAL AERONAUTICS AND SPACE ADMINISTRATION

---

For sale by the Clearinghouse for Federal Scientific and Technical Information  
Springfield, Virginia 22151 - Price \$0.90

EFFECT OF GEOMETRIC MODIFICATIONS ON THE MAXIMUM  
LIFT-DRAG RATIOS OF SLENDER WING-BODY CONFIGURATIONS  
AT HYPERSONIC SPEEDS

By William J. Small and Mitchel H. Bertram  
Langley Research Center

SUMMARY

An investigation was conducted at Mach numbers of 6.8 and 9.6 in the Langley 11-inch hypersonic tunnel to determine the effects of geometric modifications and Reynolds number on the maximum lift-drag ratio of a series of slender wing-body configurations derived from high-maximum-lift-drag-ratio arrow-wing and delta-wing-body combinations. Most of the tests were conducted with models having  $77.5^\circ$  and  $80.0^\circ$  swept wings and  $5^\circ$  cone bodies. The basic configurations were altered by clipping the wing tips, removing portions of the wing-root areas, and adding a small half-cylindrical afterbody to several configurations. These modifications were intended to increase the volume—planform-area ratio of the vehicle with little sacrifice of the maximum lift-drag ratio. Results indicated that all modifications decreased the maximum lift-drag ratio much as would be expected from volume-area considerations; however, moderate amounts of the wing tip could be removed with little decrease of the maximum lift-drag ratio. For the basic models showing favorable flow interference benefits at a Mach number of 6.8 when the body was located beneath the wing, the favorable interference continued to occur throughout the series of geometric modifications.

INTRODUCTION

The attainment of high lift-drag ratios is important to the development of extended-range hypersonic glide and cruise configurations (ref. 1). A practical means of obtaining favorable flow interference for increasing lift-drag ratios at high supersonic speeds is suggested in reference 2. In this concept, configurations benefiting from favorable flow interference generally consist of a slender body mounted beneath a thin wing (flat-top configuration), the pressure field generated by the body acting upon the wing in such a way as to improve the maximum lift-drag ratios above those of the same configuration with a midwing or a wing below the body (flat bottom). These favorable interference benefits have been found to exist on basic configurations from the supersonic into the hypersonic Mach number region (see refs. 3 to 11) where criteria involving the leading-edge shock

detachment and the volume parameter (refs. 10 and 11) are satisfied. However, at high hypersonic Mach numbers (above 10 or 11) in spite of satisfying these criteria favorable interference benefits may tend to disappear (refs. 10 and 12).

Although of importance in itself, the maximum lift-drag ratio cannot be the sole determining factor in the selection of an efficient hypersonic vehicle. The extreme aerodynamic and heat-transfer problems encountered in hypersonic flight will require a strong heat protecting, lightweight compact structure. Such a vehicle must also be stable at these speeds.

The purpose of this investigation was to determine the aerodynamic effects of modifications designed to increase the compactness of a number of basic wing-body vehicles with high-lift-drag-ratio characteristics. These basic configurations were known to have superior maximum lift-drag ratios for the flat-top configuration at a Mach number of 6.8 (ref. 11). Four basic types of vehicles were selected to be modified. The first two types consisted of an arrow wing and a delta wing having  $77.5^\circ$  leading-edge sweep in combination with a  $5^\circ$  cone body offset  $1^\circ$  from the cone axis. The third vehicle type consisted of a delta wing having  $80^\circ$  leading-edge sweep and a  $5^\circ$  cone body. The fourth type consisted of an arrow wing having  $77.4^\circ$  leading-edge sweep and a  $3/4$ -power-law body. Modifications to the arrow-wing and delta-wing-body configurations included progressive clipping of the wing tips, removal of portions of the wing-root areas, and addition of a small half-cylindrical afterbody to several configurations.

Many of the comparisons of the change in maximum lift-drag ratio between various configurations were made on the basis of change in the volume<sup>2/3</sup>-planform-area ratio, a parameter used extensively as a measure of vehicle compactness and to a lesser extent as a correlation parameter for the maximum lift-drag ratio of lifting vehicles of widely varying geometry (refs. 3 and 8 to 12). Some comparisons were also made of the effects of modifications on the location of the aerodynamic center.

All tests were performed in the Langley 11-inch hypersonic tunnel in air. Most of the tests were conducted at Mach 6.8. To provide some indication of the effect of these modifications at a higher Mach number, a few models were tested at a Mach number of 9.6.

## SYMBOLS

A	aspect ratio, $B^2/S$
B	wing span
$b_a$	wing trailing-edge sweep gap (see fig. 1(a))

$b_r$	fuselage maximum semiwidth (see fig. 1(a))
$b_t$	wing-tip width (see fig. 1(a))
$C_A$	axial-force coefficient, $\frac{\text{Axial force}}{qS}$
$C_D$	drag coefficient, $\frac{\text{Drag}}{qS}$
$C_{D,p}$	pressure drag coefficient
$C_L$	lift coefficient, $\frac{\text{Lift}}{qS}$
$C_m$	pitching-moment coefficient about the center of volume ( $x_{CV}$ , $z_O$ ), $\frac{\text{Pitching moment}}{qSl_p}$
$C_N$	normal-force coefficient, $\frac{\text{Normal force}}{qS}$
$c_c$	wing chord measured from rearmost wing-body junction to model vertex
$c_s$	length of wing leading-edge wedge in stream direction (see fig. 1(a))
$c_t$	wing-tip chord (see fig. 1(a))
$c_w$	total wing length (see fig. 1(a))
$d_n$	model nose diameter
$L/D$	lift-drag ratio
$(L/D)_{\max}$	maximum lift-drag ratio
$l_b$	total fuselage length (see fig. 1(a))
$l_h$	length of fuselage without afterbody (see fig. 1(a))
$M$	free-stream Mach number
$q$	dynamic pressure
$R$	Reynolds number based on total fuselage length $l_b$
$r$	local radius of fuselage (see fig. 1(a))

S	total planform area of model
$S_w$	planform area of wing excluding that portion subtended by fuselage (exposed wing area)
$S_{w,s}$	wing area covered by body shock (where body shock is exterior to wing leading edge, this term includes area bounded by body shock, wing span, and wing trailing edge (see fig. 12))
V	volume of model excluding volume of exposed wing
$V_t$	total volume of model including exposed wing
x	distance from model vertex in chordwise direction
$x_{ac}$	distance from model vertex to aerodynamic center in x-direction for $\alpha = 0$ , $x_{cv} - \frac{dC_m}{dC_N} z_b$
$x_{cv}$	distance from model vertex to center of volume
$z_o$	normal distance from wing surface to volume center (see fig. 1(a))
$\alpha$	angle of attack with respect to flat wing surface
$\beta$	wing trailing-edge angle (see fig. 1(a))
$\theta$	cone semivertex angle (see fig. 1(a))
$\Lambda$	wing leading-edge sweep angle
$\lambda$	taper ratio, $\frac{c_t}{c_c}$
$\tau$	fuselage offset angle (see fig. 1(a))
$\phi$	wing leading-edge wedge angle in stream direction (see fig. 1(a))

## APPARATUS AND METHODS

### Tunnel and Nozzles

Tests were conducted in the Langley 11-inch hypersonic tunnel. This blowdown facility can be operated at Mach numbers of 6.8 and 9.6 in air by changing nozzles. The Mach 6.8 nozzle is a contoured two-dimensional nozzle machined from invar to minimize deflection of the nozzle throat due to thermal gradients. The Mach 9.6 nozzle is a

contoured three-dimensional nozzle with a square throat and test section. A description of the tunnel may be found in references 13 and 14, and the calibrations of the two nozzles used are contained in references 15 and 16.

### Models

The characteristic dimensions of the wing-body models used in the investigation are given in table I. Sketches of these models are shown in figure 1. All wings were formed from a simple wedge-slab section and are of the same thickness (0.0248 cm) except for the 3/4-power body models which had a wedge-shaped airfoil. Leading edges varied from 0.05 mm to 0.08 mm in thickness. The wing surface adjacent to the body was flat for all models and was aligned with the free-stream flow for an angle of attack of 0°.

Model series 1 and 2 incorporate a half and a full 3/4-power-law body, respectively, with radius given by  $r = b_r(x/l_h)^{3/4}$  in conjunction with a 77.4° swept wing with various taper ratios. For model series 1 the bodies were cut 1° above their axes, and the wings were attached to the flat upper surfaces so formed.

Models 9, 10, 11, 13, 16, and 17 consist of a cone-type body and wings of various sweeps and taper ratios. The bodies of models 9, 10 series, 11, 13 series, and 16-3 were constructed from a cone with a 5° semiapex angle offset 1° above the cone axis. Models 16-0, 16-1, and 16-2 have 5° half-cone bodies and model 17 has a 4° half-cone body. The models were tested in both upright and inverted positions to determine their optimum attitudes.

### Force Measurements and Test Conditions

Normal force, axial force, and pitching moment were measured by an external three-component strain-gage balance, the model support sting of which was shielded from the free-stream flow to prevent any extraneous forces from acting on the balance. Model base pressure was corrected to free-stream static pressure and corresponding corrections were made to axial-force measurements. The angles of attack of all models were set by means of a light beam reflected from the model onto a calibrated scale. This method minimizes error in angle-of-attack measurements due to the deflection of the balance and sting under load. The tunnel stagnation temperatures were 616° K and 950° K for the Mach 6.8 and 9.6 tests, respectively. The absolute humidity of the air was kept sufficiently low to avoid water condensation.

### Accuracy of Data

The calculated average errors in the data for a typical test with model 10-0 at Mach 6.8 and 9.6 as a result of the uncertainties in angle of attack and Mach number and

those associated with measuring the forces, moments, and base pressures are estimated to be as follows:

	$M = 6.8; R = 1.5 \times 10^6$	$M = 9.6; R = 0.7 \times 10^6$
$C_m$ . . . . .	$\pm 0.0004$	$\pm 0.0008$
$C_L$ . . . . .	$\pm 0.0021$	$\pm 0.0016$
$C_D$ . . . . .	$\pm 0.0004$	$\pm 0.0006$
$L/D$ . . . . .	$\pm 0.25$	$\pm 0.35$

## RESULTS AND DISCUSSION

Comparisons and correlations of data are presented in figures 2 to 12. Lift, drag, and pitching-moment data for all models used in this study are presented in figures 13 to 16. The lift and drag coefficients are presented as a function of the angle of attack, and the pitching-moment coefficient is presented as a function of the normal-force coefficient. Data for flat-bottom models are shown as negative angles of attack, lift coefficients, and lift-drag ratios. All comparisons between configuration types are derived from these basic data, except as noted in figure 12.

### Effects of Reynolds Number

Most of the data shown subsequently are for Reynolds numbers (based on model body length) of  $1.5 \times 10^6$  at  $M = 6.8$  and  $0.7 \times 10^6$  at  $M = 9.6$ . In order to show generally the effects that deviations from these nominal Reynolds numbers would have on  $(L/D)_{\max}$ , several of the models were tested over a range of Reynolds number and the results are presented in figure 2. For comparison, several calculated curves are included with the experimental data. The solid-line curves represent a delta wing with zero thickness in laminar flow and with boundary-layer displacement effects. The values for these curves are from unpublished work by Bertram in which the differential equation formed by equation (7) of reference 17 with either the hypersonic shock equation or expansion equation is solved with the assumption of local hypersonic laminar boundary-layer similarity. At  $M = 9.6$  this curve has been modified by adding an arbitrary increment in drag (simulating form drag) at zero angle of attack to bring the curve into the range of the data (see dash-line curve for  $C_{D,p} = 0.0004$ ). Within the accuracy of the data the trends indicated are, as might be expected at these Reynolds numbers, those for a laminar boundary layer and this method could probably be used to extrapolate or interpolate the data so long as the flow remains laminar.

For  $M = 6.8$  in figure 2, in addition to the laminar curve a curve is shown which includes an increment in skin friction for transitional and turbulent flow, based on a fairing of the experimental skin-friction curve for thin delta wings from figure 12 of

reference 16. The lower curves have been derived from the upper curves by adding an arbitrary increment in drag coefficient. The present data, at least at the higher Reynolds number, generally indicate less of an increase in  $(L/D)_{\max}$  with increasing Reynolds number than is indicated by the calculations. This may be due to transition at a Reynolds number lower than that for the thin delta wings of reference 16, since transitional flow has been reported in reference 18 at Reynolds numbers as low as  $0.5 \times 10^6$  at a Mach number of 6.8 for models similar to the present models and tested in the same tunnel. For most models in figure 2 at  $M = 6.8$  there is found to be an advantage in  $(L/D)_{\max}$  when the body is beneath the wing (flat top) rather than above the wing (flat bottom).

### Effects of Taper Ratio

Progressive clipping of wing tips was the first method utilized for increasing the volume parameter  $\frac{V^{2/3}}{S}$ . Elimination of wing tips would remove regions of high skin friction on the wing (ref. 7). Additionally, a clipped wing would be expected to be structurally more compact than an unclipped wing. Counteracting these beneficial results, however, would be aerodynamic tip losses. The experimental results of this study are presented in figures 3(a) and 3(b) which show the variation of  $(L/D)_{\max}$  with taper ratio  $\lambda$  of all clipped-wing configurations. The maximum lift-drag ratio generally decreases slightly with increasing taper ratio, which corresponds to increasing  $\frac{V^{2/3}}{S}$ . Note that the penalty in  $(L/D)_{\max}$  for the extent of wing-tip clipping considered here is not large. As expected, the zero-taper-ratio configurations showed favorable interference benefits, or flat-top superiority, and these favorable interference benefits are preserved, for even the most extreme case of wing-tip clipping. Figure 3(c) shows a forward shift of the aerodynamic center with increasing taper ratio for all clipped-wing models tested, a result to be expected with removal of rear portions of the planform area.

Figure 4 presents the collected data from all models for which the taper ratio was progressively changed. The characteristic decrease in  $(L/D)_{\max}$  with increase in  $\frac{V^{2/3}}{S}$  (increasing taper ratio) is seen to be nearly the same for all configurations. Correlation of  $(L/D)_{\max}$  with  $\frac{V^{2/3}}{S}$  is reasonably good between closely similar models such as these.

A theoretical study of the  $(L/D)_{\max}$  variation with taper ratio was carried out for flat-top models 10-0, 13-6, 13-8, 16-1, and 16-2 at Mach 6.8. A modified theory of reference 6 was used to calculate normal force and pressure drag. The laminar reference-temperature method of reference 19 was used to calculate skin friction with an assumed model wall temperature one-half the stagnation temperature; no boundary-layer interaction effects were considered. The skin-friction drag coefficient was corrected for increasing taper ratio as described in reference 20. Normal force was corrected for taper ratio by

assuming normal-force coefficients drop to one-half the zero-taper-ratio value behind a Mach line originating from the wing-tip leading edge, as suggested by linear theory (ref. 21). This local Mach line is considered to remain constant at the zero angle-of-attack value throughout the angle-of-attack range. Figure 5 shows this theory's accuracy over a range of sweep angles for  $5^\circ$  cone bodies with  $1^\circ$  wedges. Normal- and axial-force components, the basic components of the lift-drag ratio, are first discussed for the two representative model groups studied in detail for taper-ratio effects.

Normal force.- Figure 6 shows that the normal-force coefficient remains surprisingly constant for a large range of taper ratios. As the wing tips are progressively clipped, the pressure bleed-off around the tips is apparently counterbalanced by the progressively larger proportion of high pressure field near the body cone.

Axial force.- The theoretical calculations indicate that the viscous contribution to the axial-force coefficient decreased slightly with increased taper ratio and the pressure contribution to the axial force progressively increased with reduction in planform area. As shown in figure 7 up to taper ratios of about 0.1 to 0.2, the total theoretical axial-force coefficient remains fairly constant. For taper ratios greater than about 0.1 to 0.2 the pressure drag becomes predominant and forces an upward trend in axial-force coefficient with increased taper ratio. Experimental results appear to agree with the predicted trend.

Lift-drag ratio.- Theoretical and experimental results of the  $(L/D)_{\max}$  variation with taper ratio are shown in the top plots of figure 8 for flat-top models 10-0, 13-6, 13-8, 16-1, and 16-2 at Mach 6.8. The agreement is good between theory and experiment. The curves in the bottom plots of figure 8 show the variation of experimental and theoretical lift-drag ratios with taper ratio at various angles of attack. The lift-drag ratio for all angles of attack appears to be reasonably constant up to a taper ratio between 0.1 and 0.2, as a result of the fairly constant values of normal-force and axial-force coefficients.

#### Effects of Wing-Root Modifications

Removal of wing-root area with its greater possibility of transitional and turbulent flow was expected to reduce skin-friction drag so that the value of  $(L/D)_{\max}$  would change very little. The upper plot in figure 9 indicates that models so modified showed much the same variation as the general rate of decrease of  $(L/D)_{\max}$  with increasing  $\frac{V^{2/3}}{S}$  for the overall results with flat-top configurations (dash-line curve). This general trend of  $(L/D)_{\max}$  with  $\frac{V^{2/3}}{S}$  is a graphical averaging of the data determined experimentally from similar model types (shown in fig. 11) and is included for reference only. Because of insufficient data, no conclusion can be reached for the flat-bottom configuration. The lower plot in figure 9 shows that removing wing-root area moves the

aerodynamic center forward as would be expected with wing-area removal at such a rearward position.

### Effects of Half-Cylindrical Afterbodies

Additional axial force produced by a cylindrical afterbody should be in the form of skin friction only. For this reason, small half-cylindrical afterbodies of constant length were added to a series of configurations to determine whether the volume parameter  $\frac{V^{2/3}}{S}$  would increase without significantly affecting maximum lift-drag ratio  $(L/D)_{\max}$ .

The series of configurations to which these afterbodies were added derived from an arrow-wing—body combination that had been progressively modified by reduction of wing area, in most instances by clipping the wing tips. As shown in figure 10 the addition of this afterbody decreases  $(L/D)_{\max}$  of the flat-top series approximately the same amount as would clipping the wing to achieve the same  $\frac{V^{2/3}}{S}$ . Calculations were made for two of the flat-top models to evaluate the effect on  $(L/D)_{\max}$  of these afterbodies. The assumption was made that the local cone pressure expanded at the cone-cylinder junction and this expansion produced a constant pressure over the underside of the afterbody. The afterbody top-surface pressure was assumed to be the same as the wing top-surface pressure. Skin friction was calculated as described in the section "Effects of Taper Ratio." The theory predicts a negligible variation in  $(L/D)_{\max}$  with the afterbody addition.

Figure 10 also shows that the addition of the afterbody moves the aerodynamic center forward in relation to total body length. This forward movement is expected as a result of a combination of the relative shift of the wing and the decrease in area and pressure coefficient of the cylindrical afterbody as compared with the area and pressure coefficient of the original cone-body rear section.

### Variation of Maximum Lift-Drag Ratio With Volume Parameter

Figure 11 presents the maximum lift-drag ratios of all models tested at Mach numbers of 6.8 and 9.6 at constant Reynolds numbers. As expected, a trend towards a lower lift-drag ratio with increasing  $\frac{V^{2/3}}{S}$  is evident. Data presented in reference 11 indicate that basic delta-wing—body combinations with leading-edge sweep angles between approximately  $74^\circ$  and  $82^\circ$  at a Mach number of 6.8 would be expected to show favorable interference benefits (flat-top superiority). Figure 11 shows that this trend is also true of the modified configurations at a Mach number of 6.8. No definite superiority in  $(L/D)_{\max}$  can be found from the configuration studies at  $M = 9.6$ ; however, this may be due to the low Reynolds numbers employed with the resultant low values of  $(L/D)_{\max}$  (ref. 22).

Figure 11 demonstrates that  $(L/D)_{\max}$  correlation with  $\frac{V^{2/3}}{S}$  follows the very general trends mentioned in the discussion of figure 9 but this correlation is not considered precise enough to empirically predict  $(L/D)_{\max}$  and solely on the basis of  $\frac{V^{2/3}}{S}$ .

#### General Effects of Planform and Body Modification

In an attempt to judge the relative merits of all the flat-top sharp-leading-edge configurations at  $(L/D)_{\max}$  regardless of sweep, planform, or body shape, the variation of  $(L/D)_{\max}$  with  $S_{w,s}/S_w$  is presented in figure 12. The parameter  $S_{w,s}/S_w$  is an index of the efficiency of a particular wing in utilizing the body shock formed in the local flow behind a two-dimensional wing shock at the angle of attack for  $(L/D)_{\max}$ . The conical shock was calculated by assuming the body cone was at zero incidence with respect to a two-dimensional flow field beneath the delta wing at angle of attack (ref. 23). From considerations leading to the proposal of the flat-top configuration as an efficient lifting configuration (ref. 2), this area ratio should be an important parameter. A smaller value of  $\frac{V^{2/3}}{S}$  for a particular value of  $S_{w,s}/S_w$  tends to increase  $(L/D)_{\max}$ . An examination of figure 12 shows some exceptions to the trend mentioned, especially for values of  $S_{w,s}/S_w$  greater than 1 for which the definition is arbitrary. For configurations having the same value of  $\frac{V^{2/3}}{S}$  the maximum lift-drag ratio appears to peak at a value of  $S_{w,s}/S_w$  somewhat less than 1. This may indicate that the assumed body shock has been underestimated since a value of 1 for  $S_{w,s}/S_w$  (where the body shock lies along the wing leading edge) would be expected to be the most efficient condition (ref. 2); however, only the data correlations faired by the solid lines can be believed with some certainty. The dashed continuation of this curve is thought to represent a reasonable fairing of the data trends. The rough correlation of data, however, does provide an indication of the penalties encountered when a configuration is designed for other than optimum  $S_{w,s}/S_w$ .

#### CONCLUDING REMARKS

An investigation was undertaken in the Langley 11-inch hypersonic tunnel at Mach numbers of 6.8 and 9.6 in air to determine the effects of geometric modifications on the maximum lift-drag ratio of a series of slender wing-body configurations derived from high-maximum-lift-drag-ratio arrow-wing and delta-wing-body combinations. These models were tested with the wing above the body (flat-top configuration) and below the body (flat-bottom configuration); a few tests with the midwing arrangement were also made. An analysis of the results has led to the following observations:

For the basic models showing maximum-lift-drag-ratio  $((L/D)_{\max})$  superiority in the flat-top position, modifications by removal of wing-root area, addition of a small half-cylindrical afterbody, and clipping of wing tips all preserved this flat-top superiority.

All three configuration modifications (clipping of wing tips, removal of wing-root areas, and addition of a cylindrical afterbody) cause a reduction in the maximum lift-drag ratio much as would be expected from volume-area considerations. However, moderate amounts of the wing could be removed without significantly affecting the lift-drag ratio, apparently because the effect on the volume parameter  $\left(\frac{V^{2/3}}{S}\right)$  of wing-tip clipping is small unless relatively large portions of the wing tips are removed.

By taking into account the area of a wing covered by the body shock of a sharp-leading-edge flat-top configuration, a rough correlation of  $(L/D)_{\max}$  at each value of  $\frac{V^{2/3}}{S}$  was obtained irrespective of the wing planform geometry. Regardless of the manner in which various modifications were performed,  $(L/D)_{\max}$  for a given value of  $\frac{V^{2/3}}{S}$  was estimated to occur when the calculated cone shock coincided approximately with the wing leading edge.

Langley Research Center,  
National Aeronautics and Space Administration,  
Langley Station, Hampton, Va., November 24, 1965.

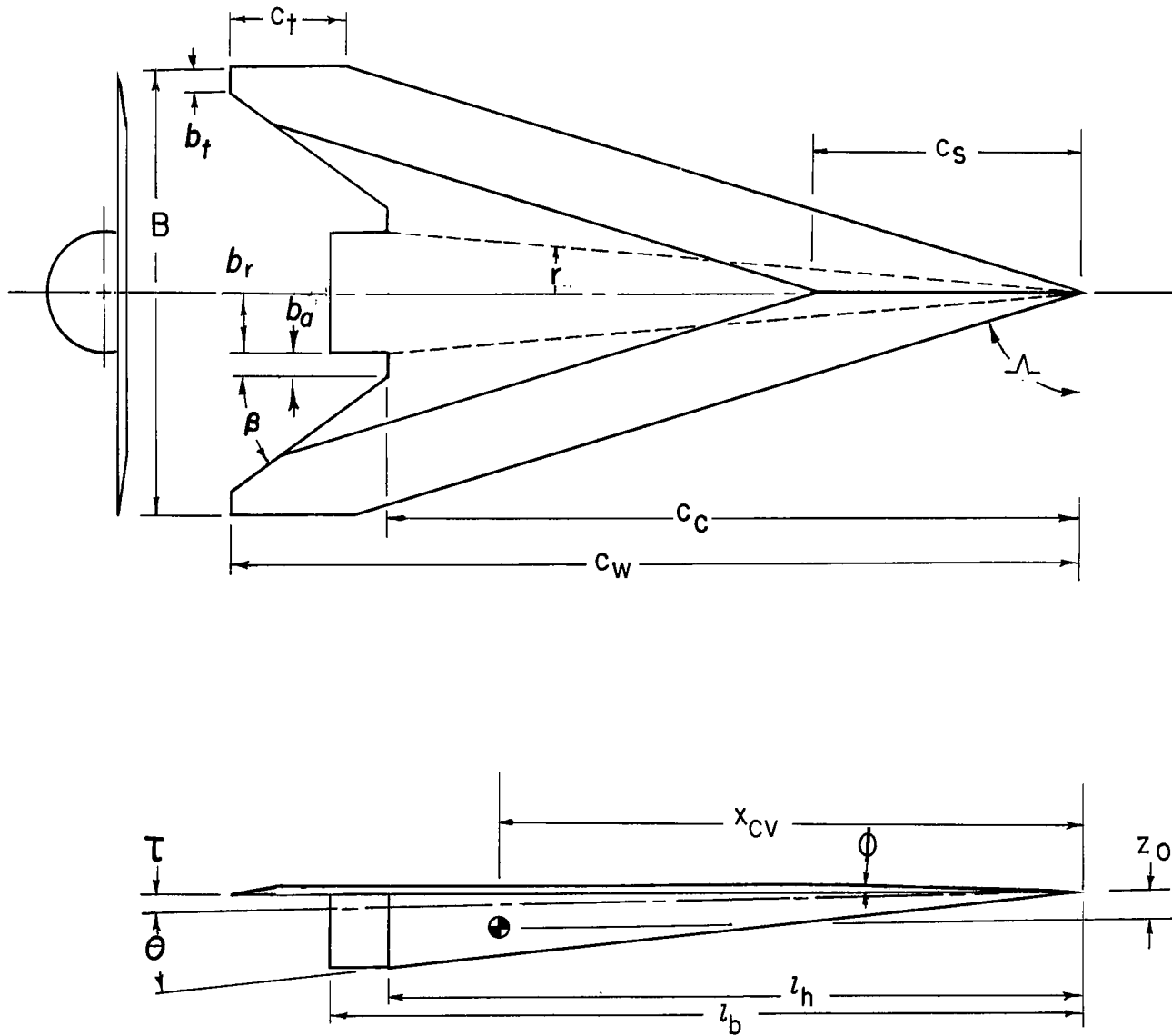
## REFERENCES

1. Eggers, Alfred J., Jr.; Allen, H. Julian; and Neice, Stanford E.: A Comparative Analysis of the Performance of Long-Range Hypervelocity Vehicles. NACA Rept. 1382, 1958. (Supersedes NACA TN 4046.)
2. Eggers, A. J., Jr.; and Syvertson, Clarence A.: Aircraft Configurations Developing High Lift-Drag Ratios at High Supersonic Speeds. NACA RM A55L05, 1956.
3. Becker, John V.: Studies of High Lift/Drag Ratio Hypersonic Configurations. Proceedings of the 4th Congress of the International Council of the Aeronautical Sciences, Robert R. Dexter, ed., Spartan Books, Inc., 1965, pp. 877-910.
4. Syvertson, Clarence A.; Wong, Thomas J.; and Gloria, Hermilo R.: Additional Experiments With Flat-Top Wing-Body Combinations at High Supersonic Speeds. NACA RM A56I11, 1957.
5. Savin, Raymond C.: Approximate Solutions for the Flow About Flat-Top Wing-Body Configurations at High Supersonic Airspeeds. NACA RM A58F02, 1958.
6. Armstrong, William O.; and Ladson, Charles L. (With appendix A by Donald L. Baradell and Thomas A. Blackstock): Effects of Variation in Body Orientation and Wing and Body Geometry on Lift-Drag Characteristics of a Series of Wing-Body Combinations at Mach numbers From 3 to 18. NASA TM X-73, 1959.
7. McLellan, Charles H.; and Dunning, Robert W.: Factors Affecting the Maximum Lift-Drag Ratio at High Supersonic Speeds. NACA RM L55L20a, 1956.
8. McLellan, Charles H.; and Ladson, Charles L.: A Summary of the Aerodynamic Performance of Hypersonic Gliders. NASA TM X-237, 1960.
9. Goebel, T. P.; Martin, J. J.; and Boyd, J. A.: Factors Affecting Lift-Drag Ratios at Mach Numbers From 5 to 20. AIAA J., vol. 1, no. 3, Mar. 1963, pp. 640-650.
10. Fetterman, David E.; Henderson, Arthur, Jr.; Bertram, Mitchel H.; and Johnston, Patrick J.: Studies Relating to the Attainment of High Lift-Drag Ratios at Hypersonic Speeds. NASA TN D-2956, 1965.
11. Fetterman, David E.: Favorable Interference Effects on Maximum Lift-Drag Ratios of Half-Cone Delta-Wing Configurations at Mach 6.86. NASA TN D-2942, 1965.
12. Johnston, Patrick J.; Snyder, Curtis D.; and Witcofski, Robert D.: Maximum Lift-Drag Ratios of Delta-Wing—Half-Cone Combinations at a Mach Number of 20 in Helium. NASA TN D-2762, 1965.
13. McLellan, Charles H.; Williams, Thomas W.; and Bertram, Mitchel H.: Investigation of a Two-Step Nozzle in the Langley 11-Inch Hypersonic Tunnel. NACA TN 2171, 1950.

14. McLellan, Charles H.; Williams, Thomas W.; and Beckwith, Ivan E.: Investigation of the Flow Through a Single-Stage Two-Dimensional Nozzle in the Langley 11-Inch Hypersonic Tunnel. NACA TN 2223, 1950.
15. Bertram, Mitchel H.: Exploratory Investigation of Boundary-Layer Transition on a Hollow Cylinder at a Mach Number of 6.9. NACA Rept. 1313, 1957. (Supersedes NACA TN 3546.)
16. Bertram, Mitchel H.: Boundary-Layer Displacement Effects in Air at Mach Numbers of 6.8 and 9.6. NASA TR R-22, 1959. (Supersedes NACA TN 4133.)
17. Bertram, Mitchel H.; and Blackstock, Thomas A.: Some Simple Solutions to the Problem of Predicting Boundary-Layer Self-Induced Pressures. NASA TN D-798, 1961.
18. Dunavant, James C.: Heat Transfer to a Delta-Wing—Half-Cone Combination at Mach Numbers of 7 and 10. NASA TN D-2199, 1964.
19. Monaghan, R. J.: An Approximate Solution of the Compressible Laminar Boundary Layer on a Flat Plate. R & M No. 2760, British A.R.C., 1953.
20. Bertram, Mitchel H.: Calculations of Compressible Average Turbulent Skin Friction. NASA TR R-123, 1962.
21. Liepmann, H. W.; and Roshko, A.: Elements of Gasdynamics. John Wiley & Sons, Inc., c.1957.
22. Bertram, Mitchel H.; Fetterman, David E., Jr.; and Henry, John R.: Proceedings of the NASA-University Conference on the Science and Technology of Space Exploration, Vol. 2, NASA SP-11, 1962, pp. 215-234. (Also available as NASA SP-23.)
23. Bertram, Mitchel H.: Correlation Graphs for Supersonic Flow Around Right Circular Cones at Zero Yaw in Air as a Perfect Gas. NASA TN D-2339, 1964.

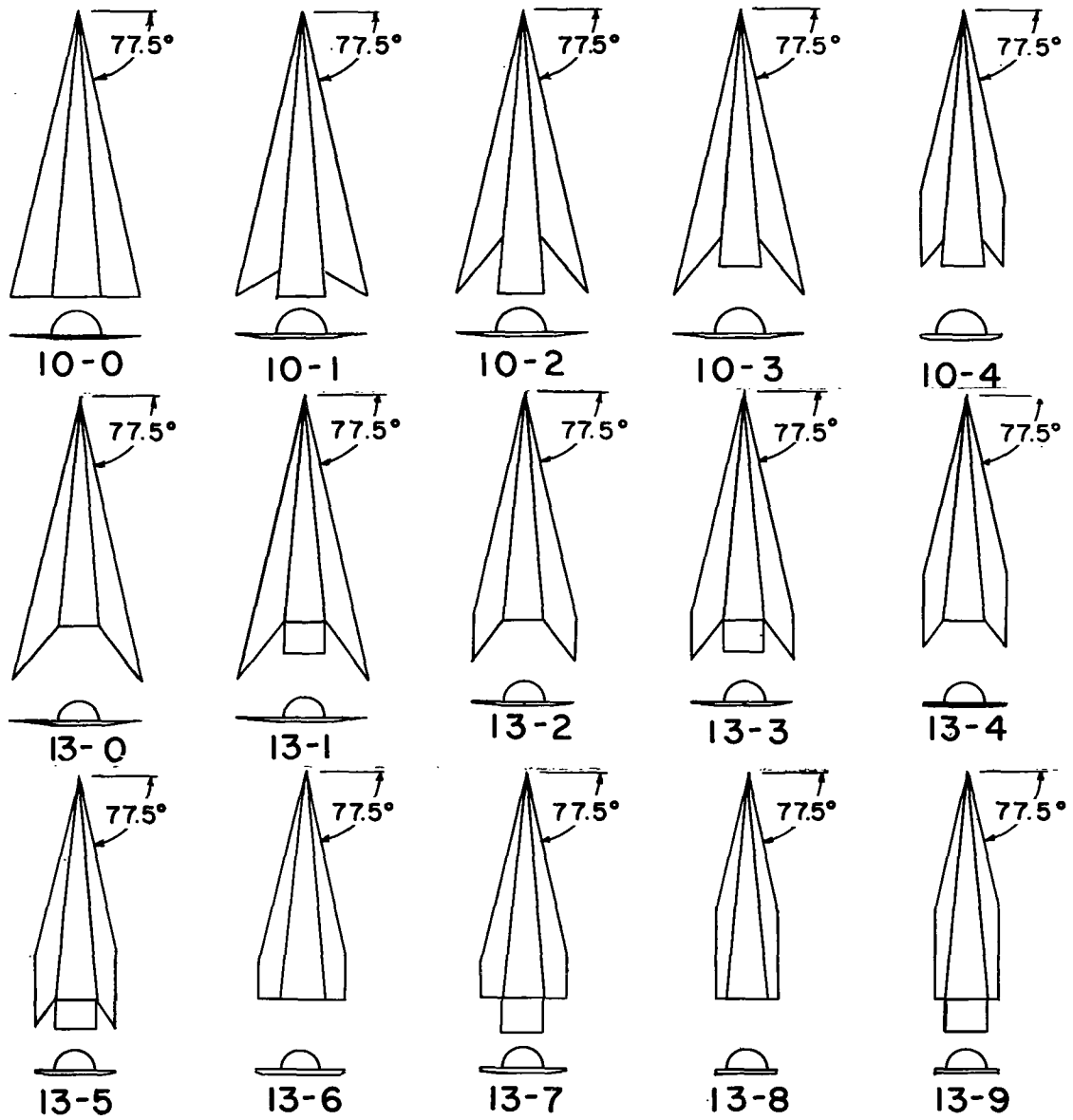
TABLE I.- CHARACTERISTIC DIMENSIONS AND PARAMETERS OF SLENDER WING-BODY MODELS

Model	$\Lambda$ , deg	$\theta$ , deg	$\tau$ , deg	$\beta$ , deg	$\phi$ , deg	$c_t$ , cm	$c_w$ , cm	$c_c$ , cm	$c_s$ , cm	$l_b$ , cm	$l_h$ , cm	$b_r$ , cm	$b_a$ , cm	$b_t$ , cm	$S$ , cm <sup>2</sup>	$B$ , cm	$x_{cy}$ , cm	$z_o$ , cm	$d_n$	$\frac{V^{2/3}}{S}$	$\frac{V_t^{2/3}}{S}$	A	Basic data figures for -				
																							M = 6.8			M = 9.6	
																							$C_L$ , L/D	$C_D$ , L/D	$C_m$	$C_L$ , L/D	$C_D$ , L/D
1-0	77.4	---	1	18	1	0	25.20	17.78	25.20	20.00	17.78	1.572	0.50	1.27	104.25	11.28	14.06	0.577	0.102	0.1379	0.1528	1.220	14(a)	16(a)	13(a)	15(a)	
1-1				19			8.48	21.08					.28	0	80.77	6.07				.1780	.1920	.456	14(b)	16(a)	13(b)	15(a)	
1-2				90			5.16	17.78					0	0	78.12	6.07				.1840	.1965	.472	14(c)	16(a)	13(c)	15(a)	
2-0			0	18		0	25.20		25.20			1.36	.74	1.27	103.73	11.28		0		.1386	.1598	1.226	14(a)	16(a)	13(a)	15(a)	
2-2				19			8.48	21.08					.50	0	80.31	6.07				.1792	.2008	.459	14(b)	16(a)	13(b)	15(a)	
2-3				90			5.16	17.78					0		77.61	6.07				.1852	.2062	.475	14(c)	16(a)	13(c)	15(a)	
9	72.0	5	1		1.48	0	15.62	15.62	8.59	15.62	15.62	1.36			79.41	10.16	11.56	.506	0	.1003	.1147	1.300	14(n)	16(e)	13(g)	15(b)	
10-0	77.5				1.04		22.91	22.91		22.91	22.91	2.01			116.51	5.08	16.95	.784		.1425	.1495	.221	14(d)	16(b)	13(d)	15(b)	
10-1				62.3					21.23						111.15		16.92			.1495	.1561	.232	14(d)	16(b)			
10-2				37.2					18.42						102.89		16.92			.1615	.1674	.251	14(e)	16(b)			
10-3										20.57	20.57	1.80			94.57		15.23	.728		.1428	.1501	.273	14(e)	16(b)			
10-4						5.87	20.57			20.57	20.57	1.80			83.86	3.24	15.23	.728		.1600	.1681	.125	14(f)	16(b)	13(d)	15(b)	
11	81			90	.75	0	32.00	32.00		32.00	32.00	2.79			162.95	10.16	23.67	1.232		.1948	.2020	.633	14(f)	16(b)	13(e)	15(b)	
13-0	77.5			37.2	1.04		22.73	18.14		18.14	18.14	1.59			84.77		13.42	.587		.1250	.1428	1.218	14(g)	16(c)	13(e)	15(b)	
13-1							22.73			20.73					93.02		14.77	.034		.1425	.1604	1.109	14(g)	16(c)			
13-2						3.25	21.39			18.14					81.41	8.11	13.41			.1306	.1471	.807	14(h)	16(c)			
13-3						3.25	21.39			20.73					89.67	8.11	14.74			.1478	.1612	.733	14(h)	16(c)			
13-4						5.59	20.24			18.14					74.44	6.56	13.74			.1424	.1622	.578	14(i)	16(c)			
13-5						5.59	20.24			20.73					82.57		14.74			.1605	.1766	.521	14(i)	16(c)			
13-6				90		3.45	18.14			18.14					71.09		13.41			.1490	.1692	.605	14(j)	16(d)			
13-7						3.45				20.73					79.28		14.74			.1673	.1839	.542	14(j)	16(d)			
13-8						7.77				18.14					59.99	4.63	13.41			.1768	.1940	.357	14(k)	16(d)	13(f)	15(b)	
13-9						7.77				20.73					68.25	4.63	14.74			.1945	.2089	.314	14(k)	16(d)	13(f)	15(b)	
16-0	80.0		0	24.6		0	21.39	16.26	8.64	16.26	16.26	1.42			53.99	7.54	11.96	.386		.1402	.1690	1.054	14(l)	16(d)			
16-1				90		0	16.26								46.64	5.73				.1621	.1652	.704	14(l)	16(d)			
16-2						3.68									44.19	4.43				.1712	.1737	.445	14(m)	16(e)			
16-3				1		3.68									44.19	4.43	12.00	.521		.1940	.1970	.445	14(m)	16(e)			
17	80.4	4	0			0			8.71			1.14			44.77	5.50	11.92	.268		.1292	.1350	.675	14(n)	16(e)			



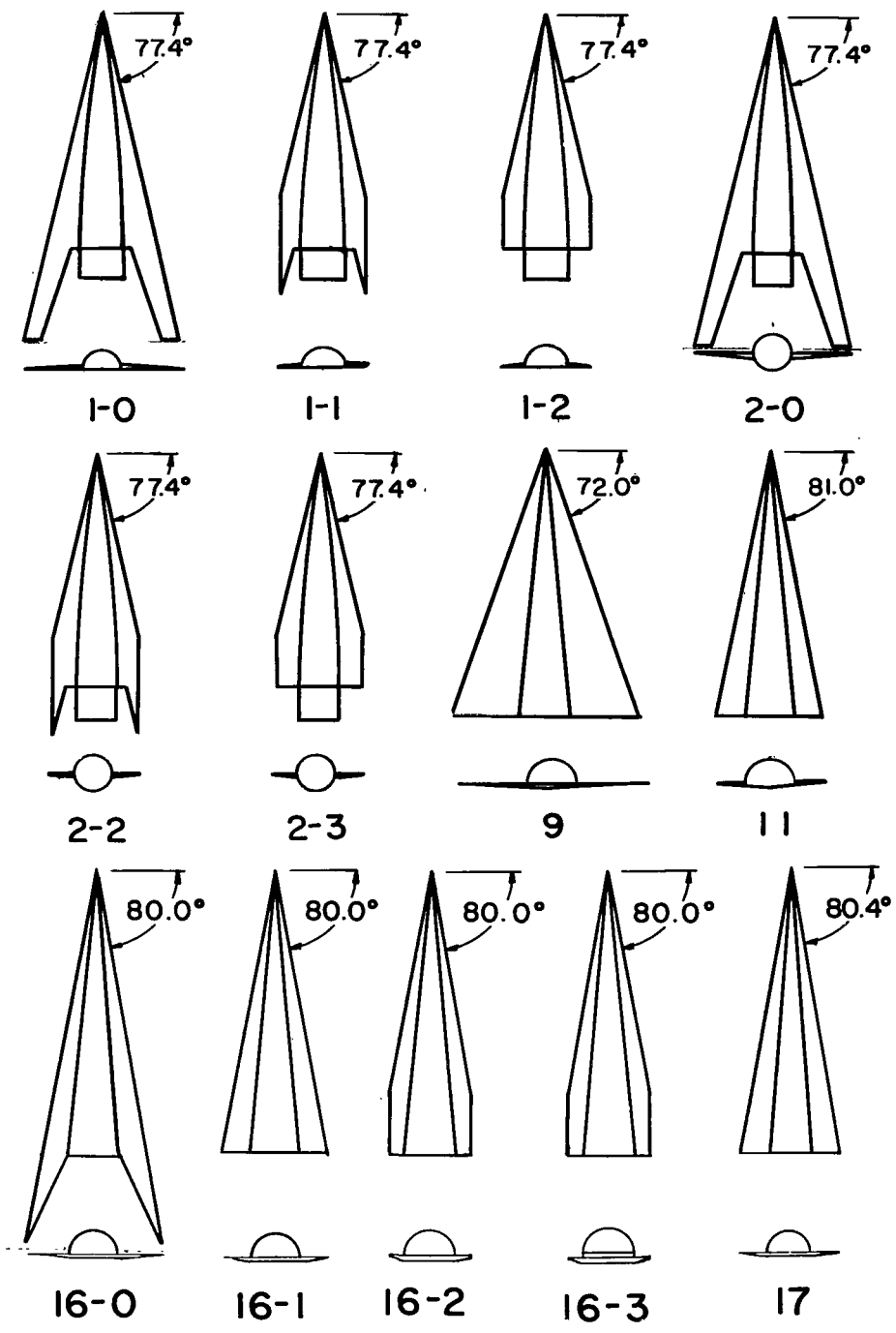
(a) Model dimensions.

Figure 1.- Slender wing-body models used in the investigation.



(b) Sketches of models tested.

Figure 1.- Continued.



(b) Concluded.

Figure 1- Concluded.

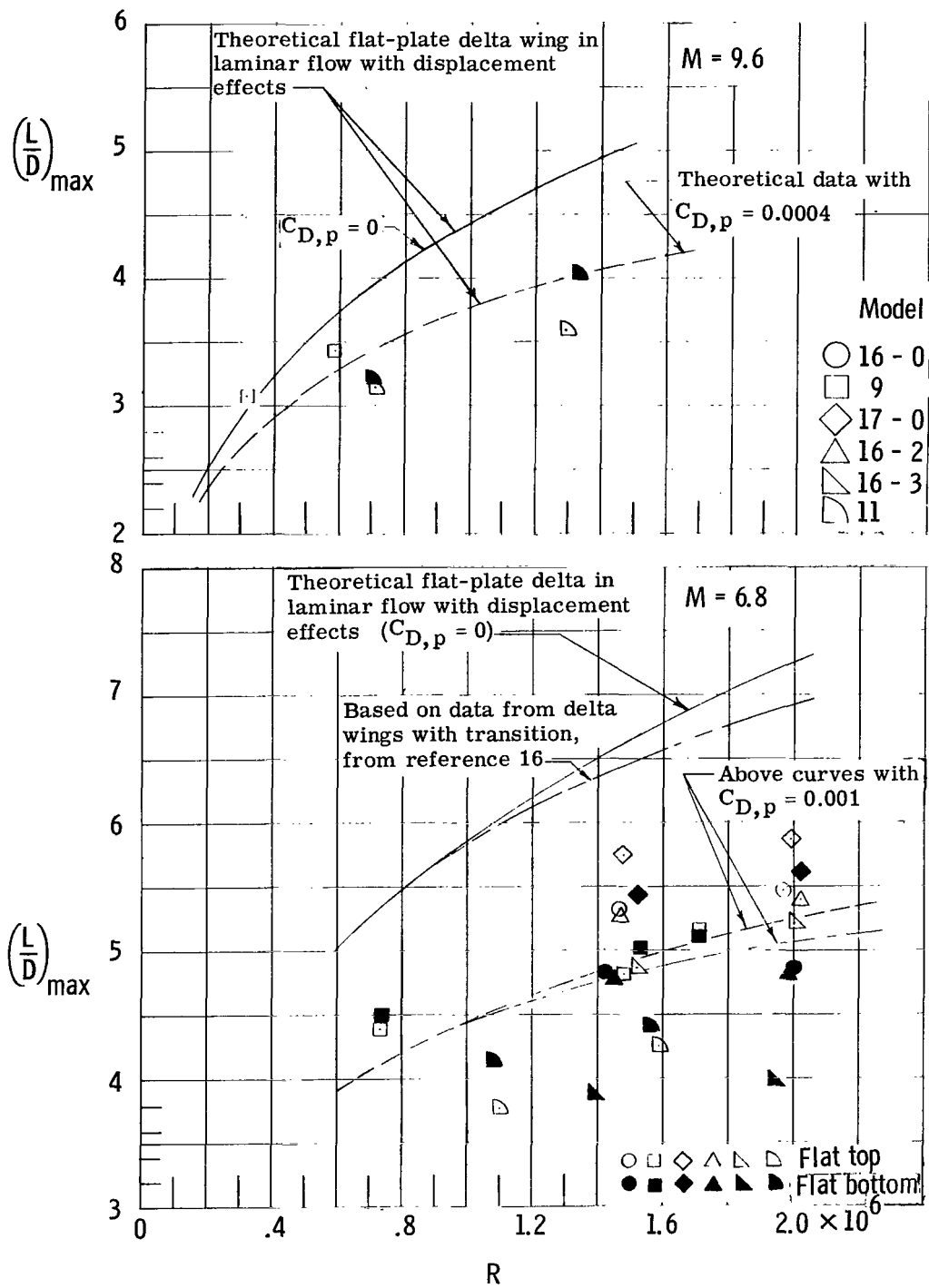
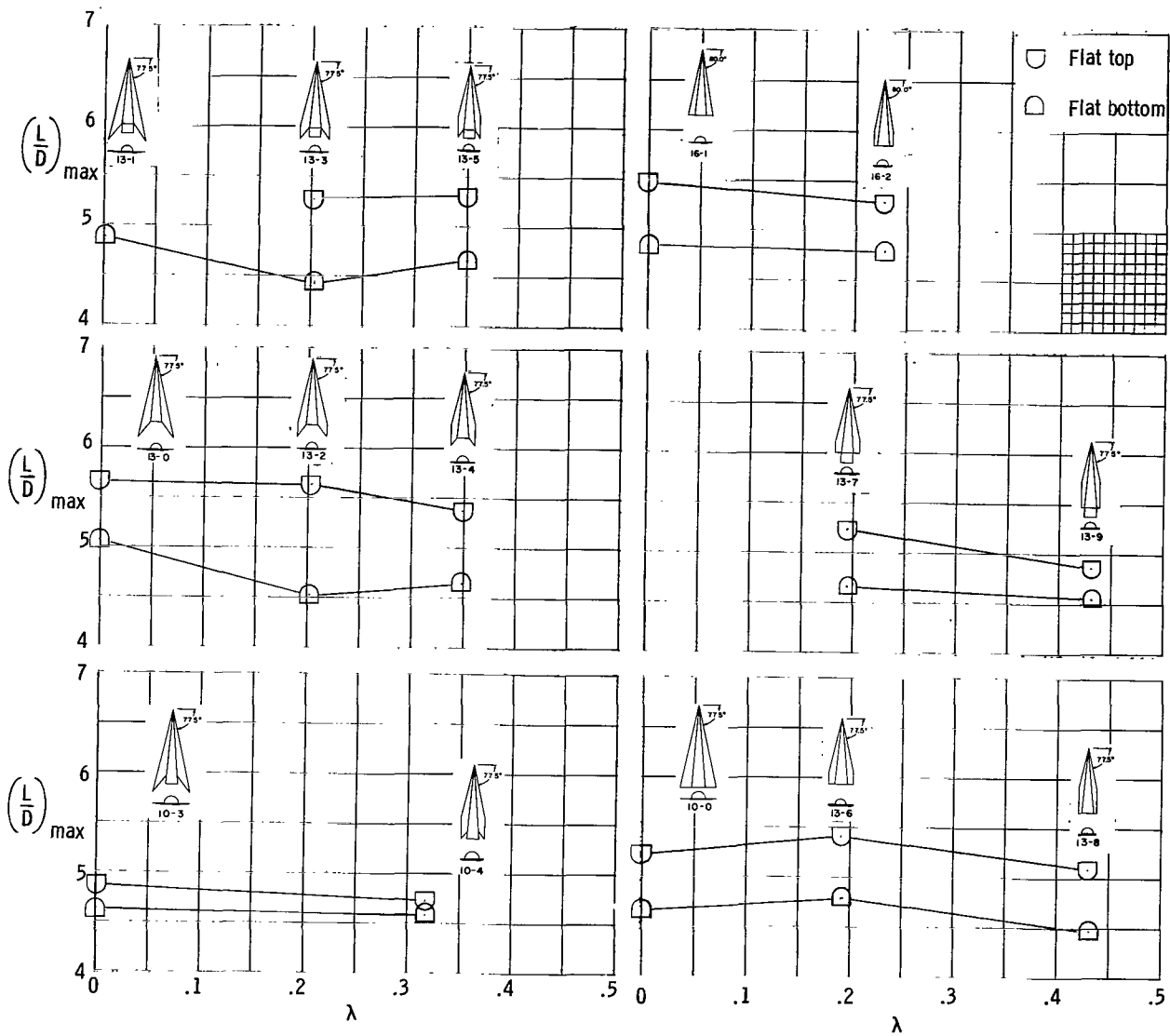
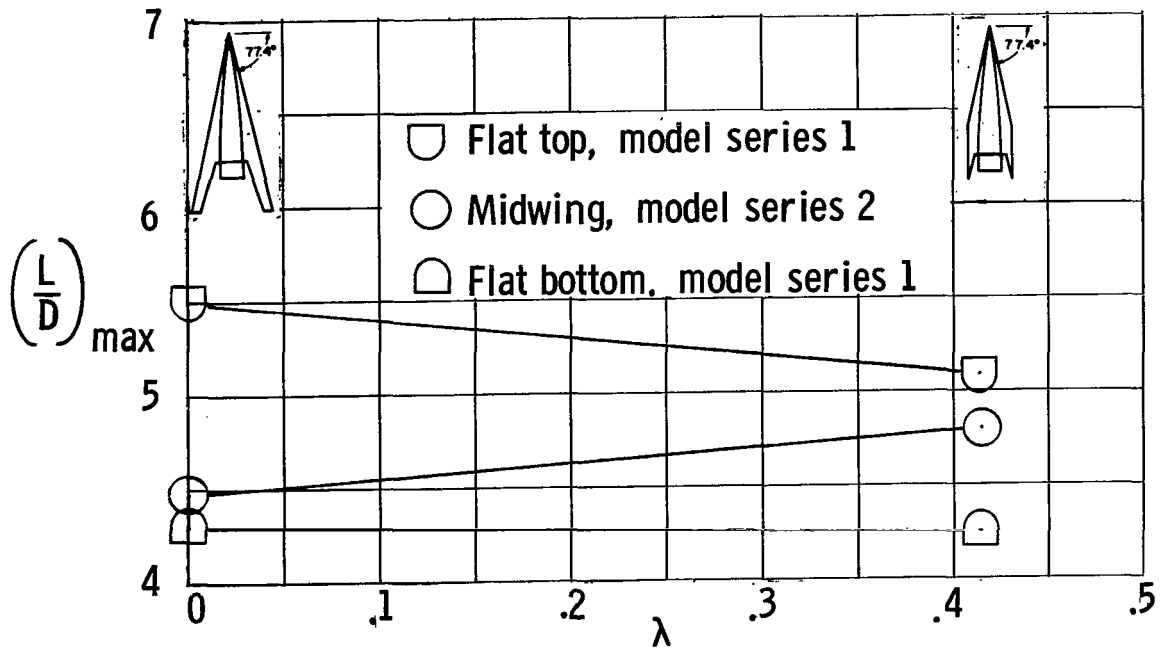


Figure 2.- Variation of  $(L/D)_{max}$  with Reynolds number.



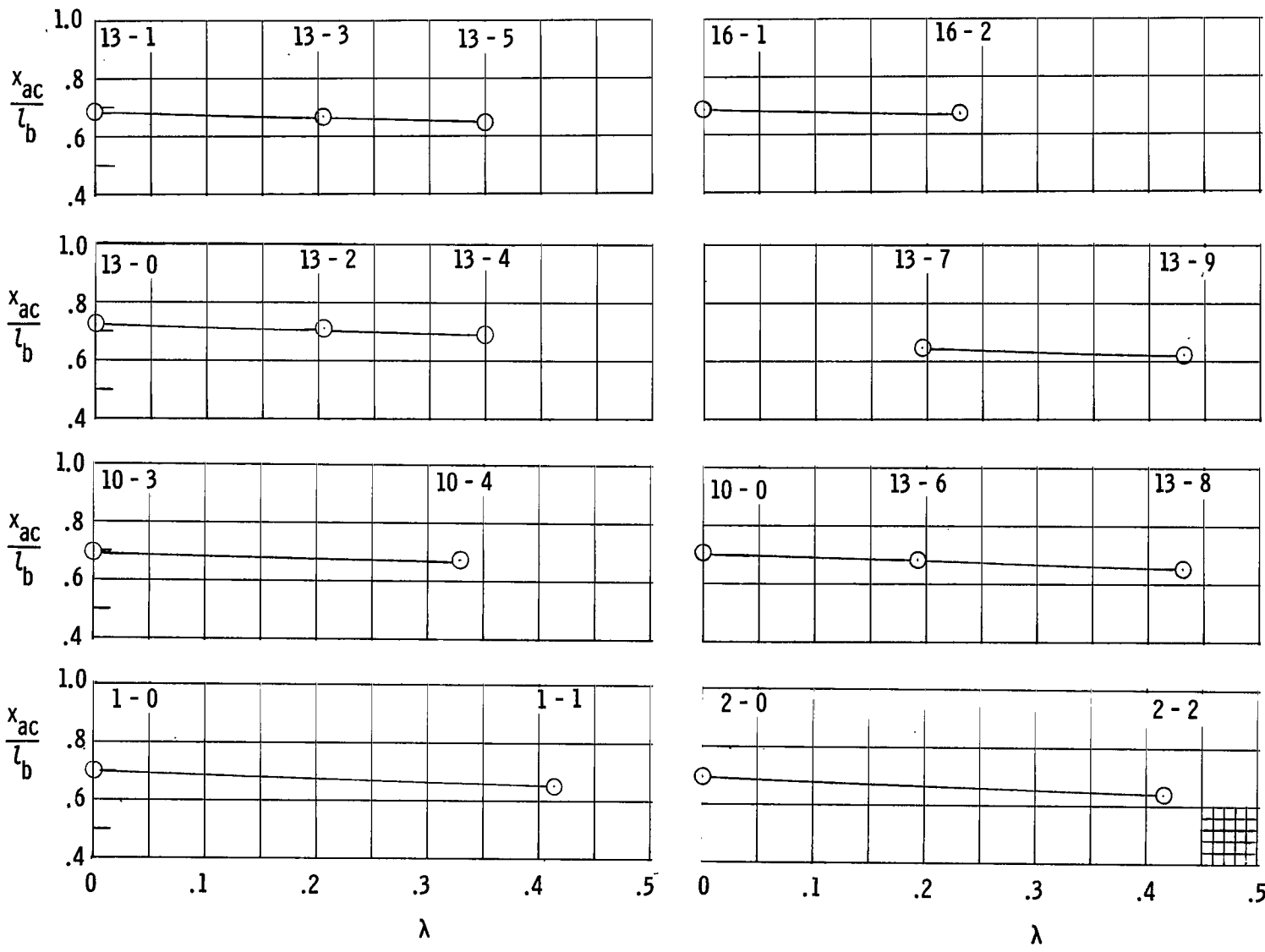
(a) Conical-body configurations.

Figure 3.- Effect of taper ratio on maximum lift-drag ratio and aerodynamic-center location.  $R = 1.5 \times 10^6$ ;  $M = 6.8$ .



(b) 3/4-power-law-body configurations.

Figure 3.- Continued.



(c) Aerodynamic-center location.

Figure 3.- Concluded.

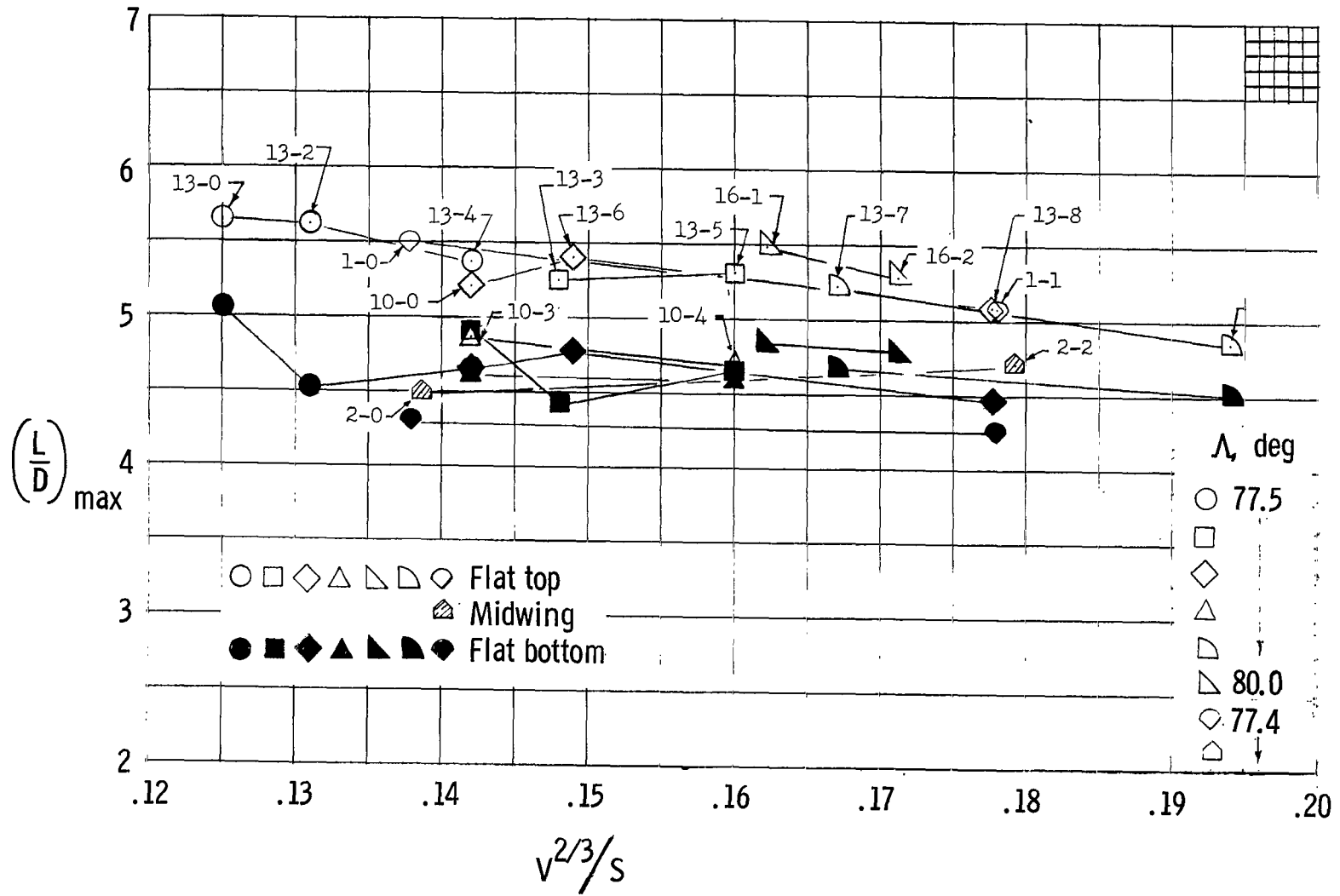


Figure 4.- Trend of maximum lift-drag ratio with volume parameter for a series of configurations with varying taper ratio.  $R = 1.5 \times 10^6$ ;  $M = 6.8$ .

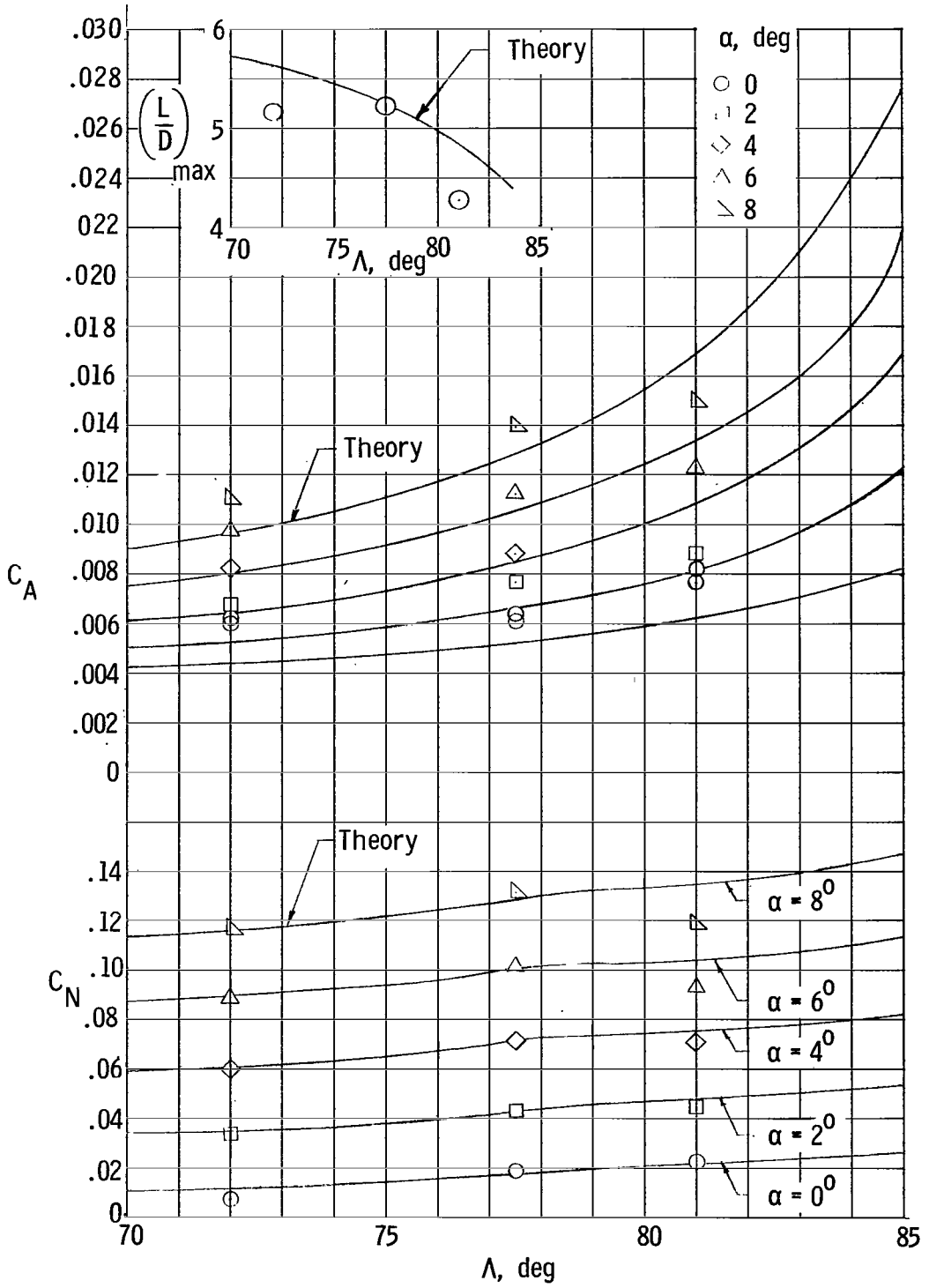
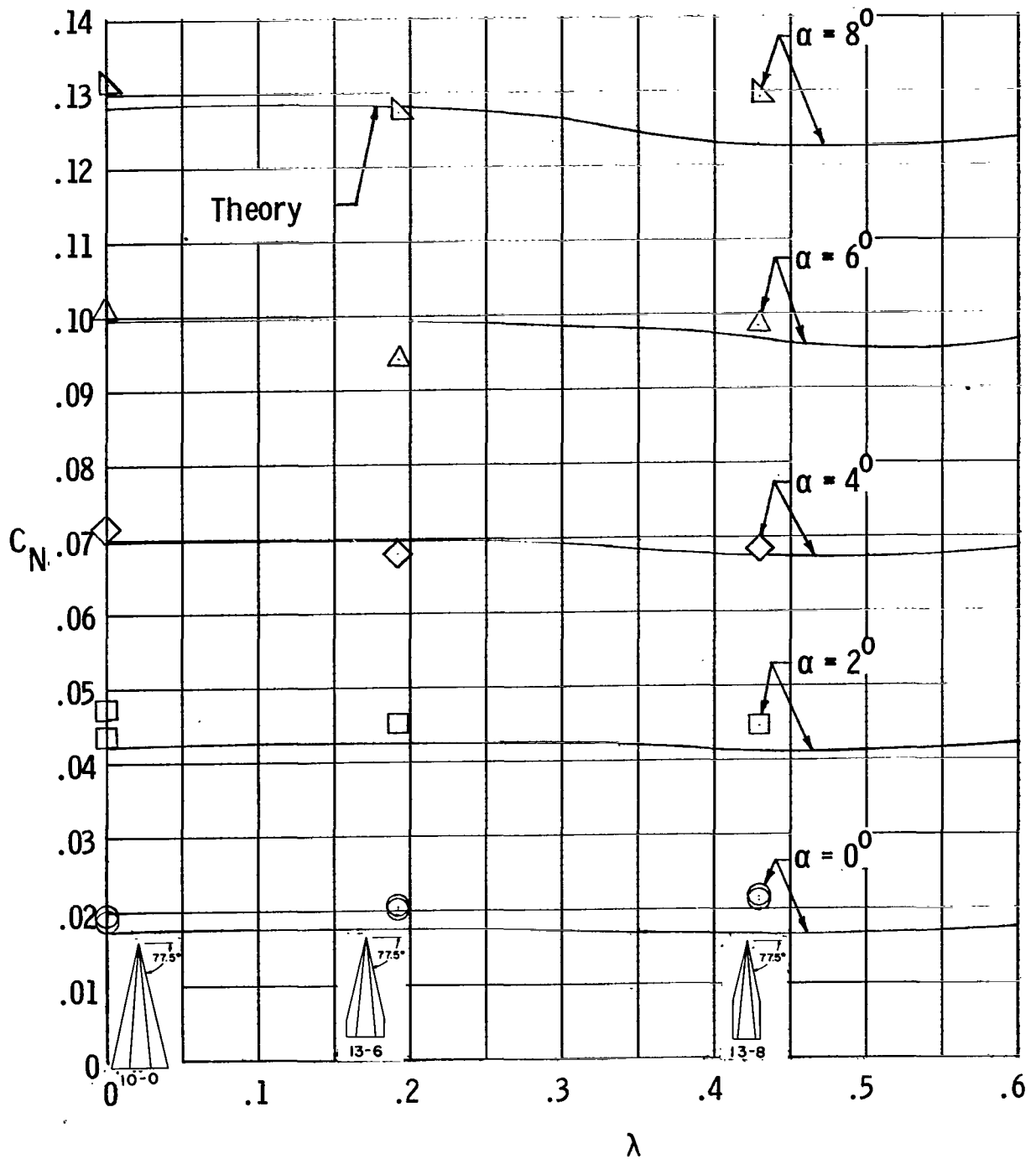
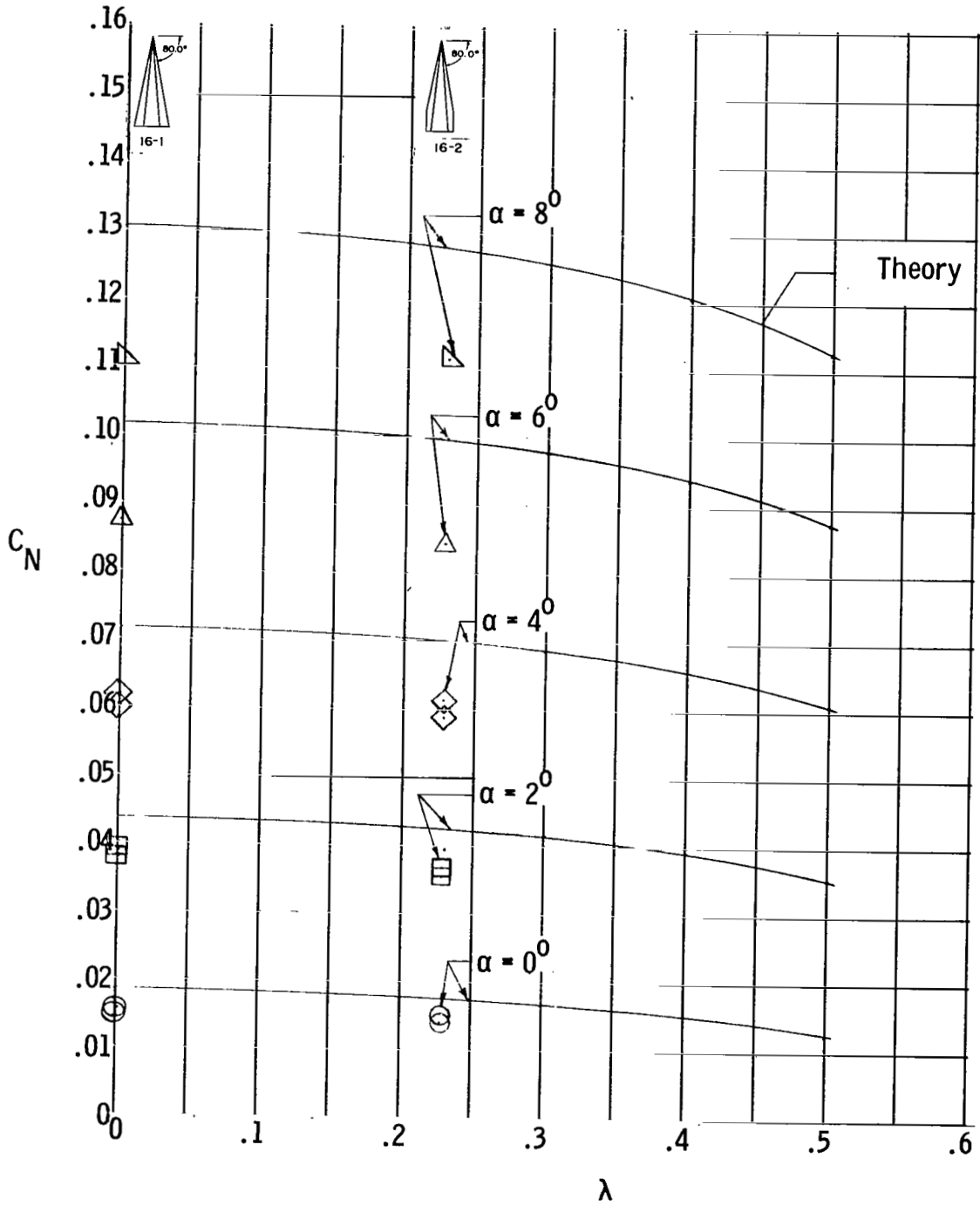


Figure 5.- Variation of  $C_A$ ,  $C_N$ , and  $(L/D)_{max}$  of a delta-wing model with sweep angle.  $\theta = 5^\circ$ ;  $\tau = 1^\circ$ ;  $R = 1.5 \times 10^6$ ;  $M = 6.8$ .



(a)  $\theta = 5^\circ$ ;  $\tau = 1^\circ$ ;  $\Lambda = 77.5^\circ$ .

Figure 6.- Variation of theoretical and experimental normal-force coefficients with taper ratio for flat-top models.  $R = 1.5 \times 10^6$ ;  $M = 6.8$ .



(b)  $\theta = 5^\circ$ ;  $\tau = 0^\circ$ ;  $\Lambda = 80.0^\circ$ .

Figure 6.- Concluded.

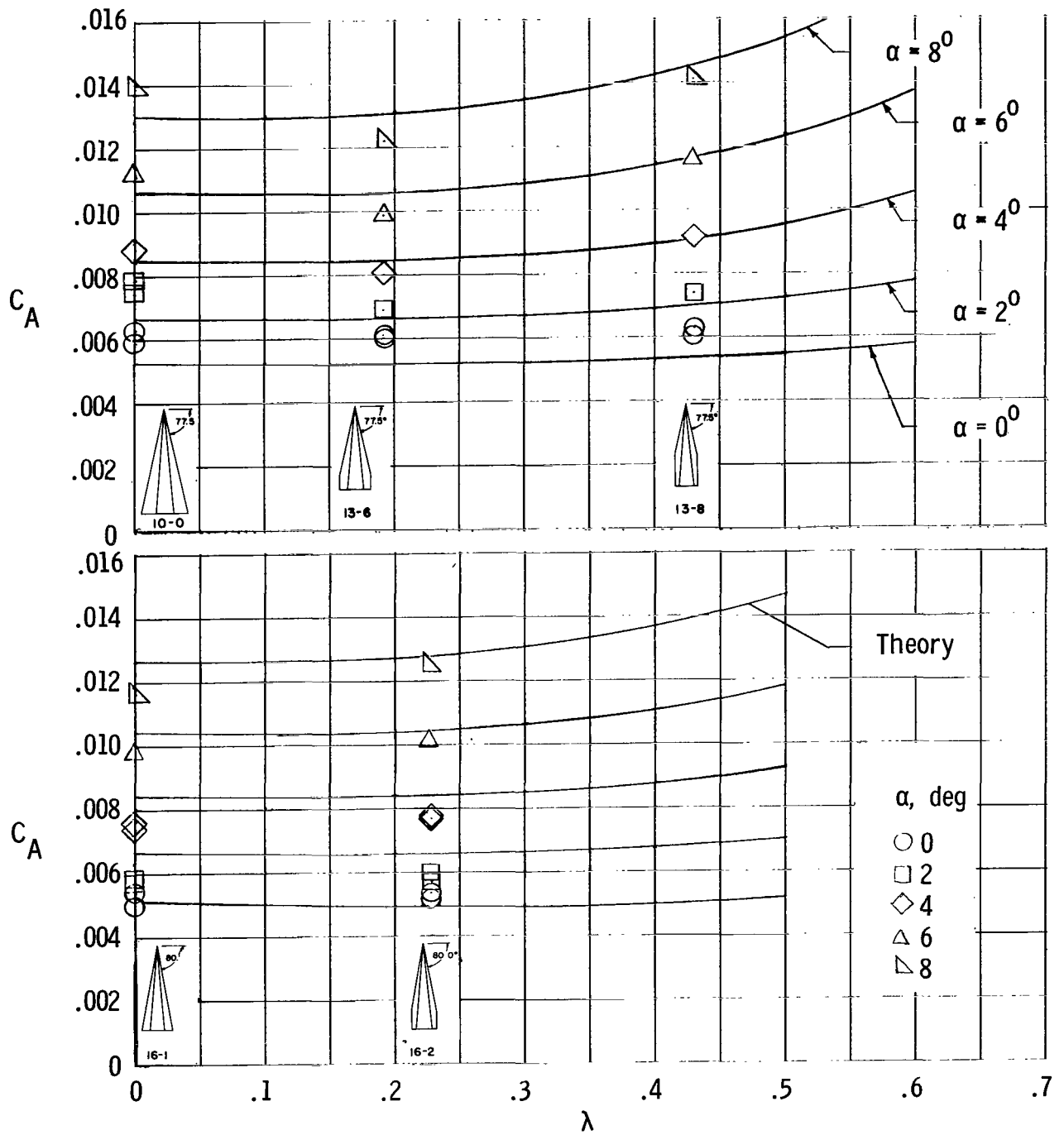
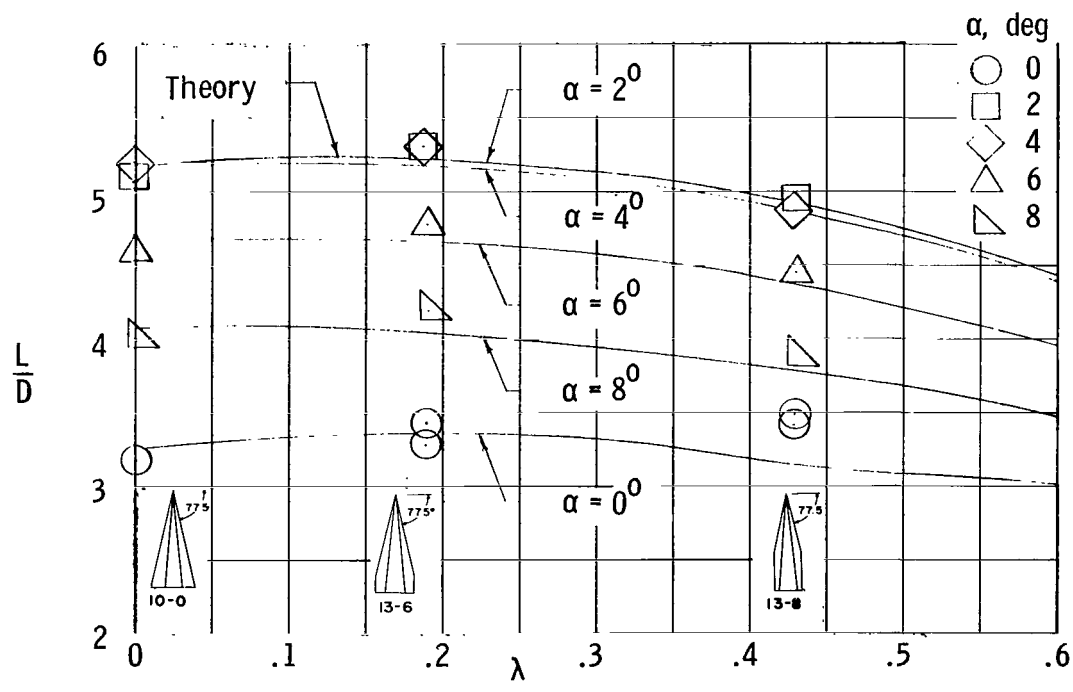
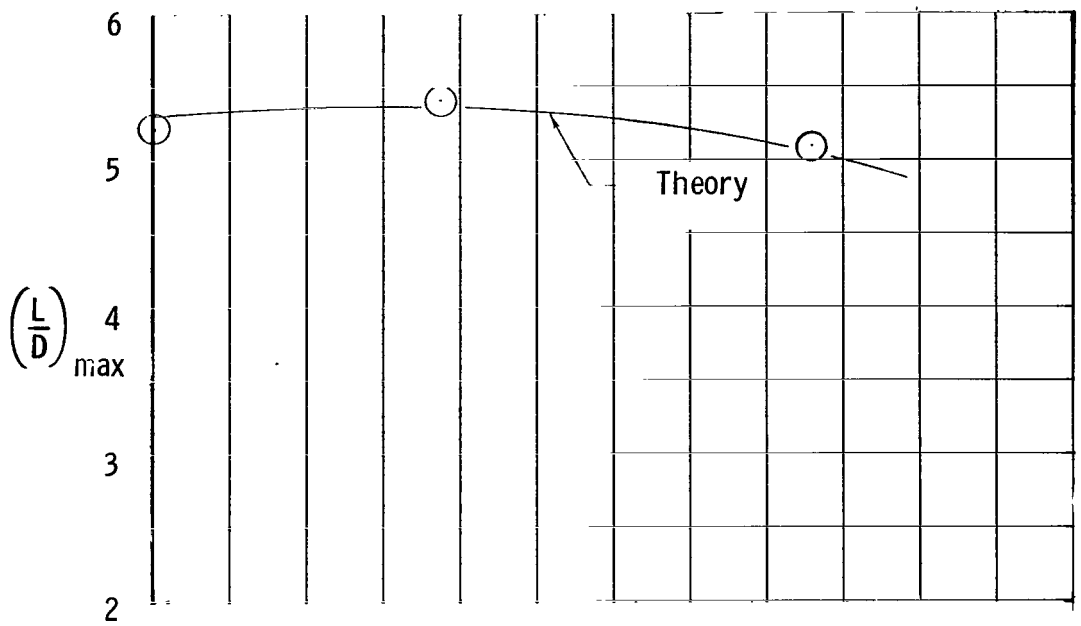
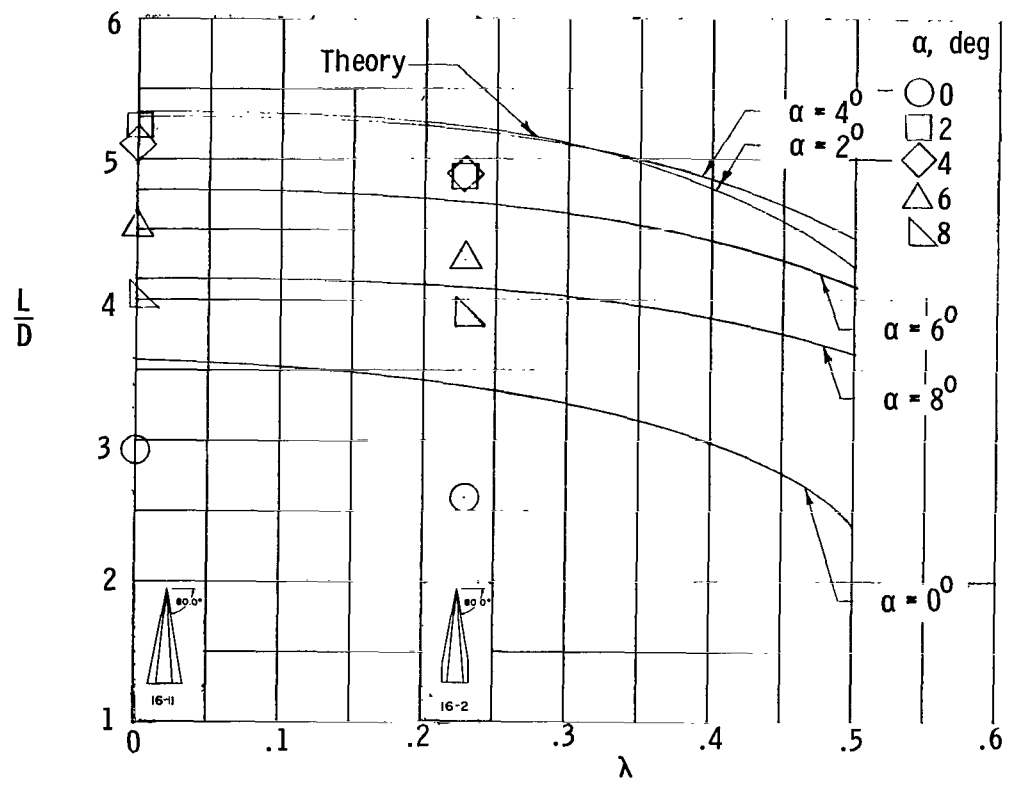
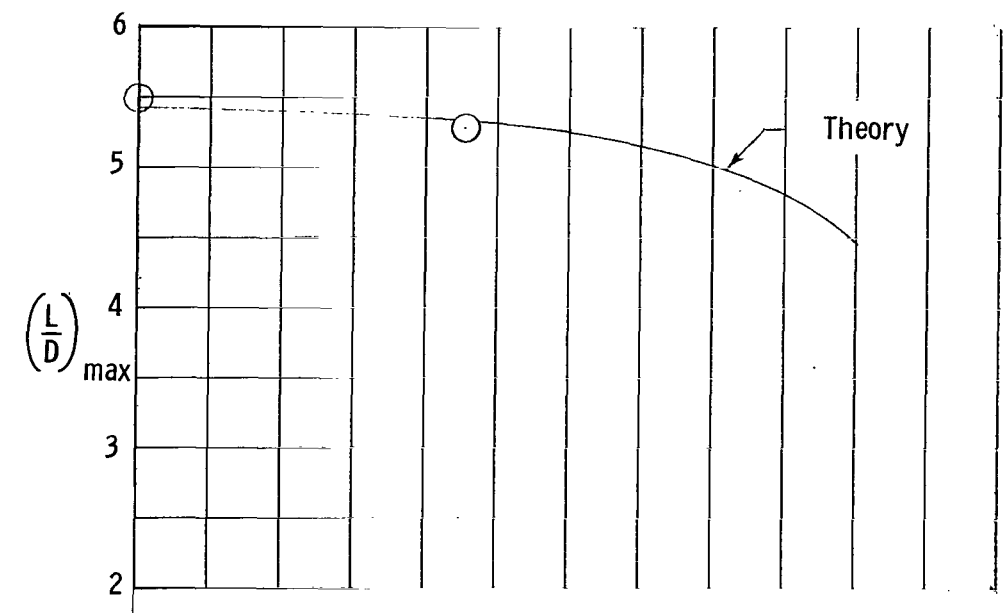


Figure 7.- Variation of theoretical and experimental axial-force coefficients with taper ratio for flat-top models.  $R = 1.5 \times 10^6$ ;  $M = 6.8$ .



(a)  $\theta = 5^\circ$ ;  $\tau = 1^\circ$ ;  $\Lambda = 77.5^\circ$ .

Figure 8.- Variation of lift-drag ratio and maximum lift-drag ratio with taper ratio for flat-top models.  $R = 1.5 \times 10^6$ ;  $M = 6.8$ .



(b)  $\theta = 5^\circ$ ;  $\tau = 0^\circ$ ;  $\Lambda = 80.0^\circ$ .

Figure 8.- Concluded.

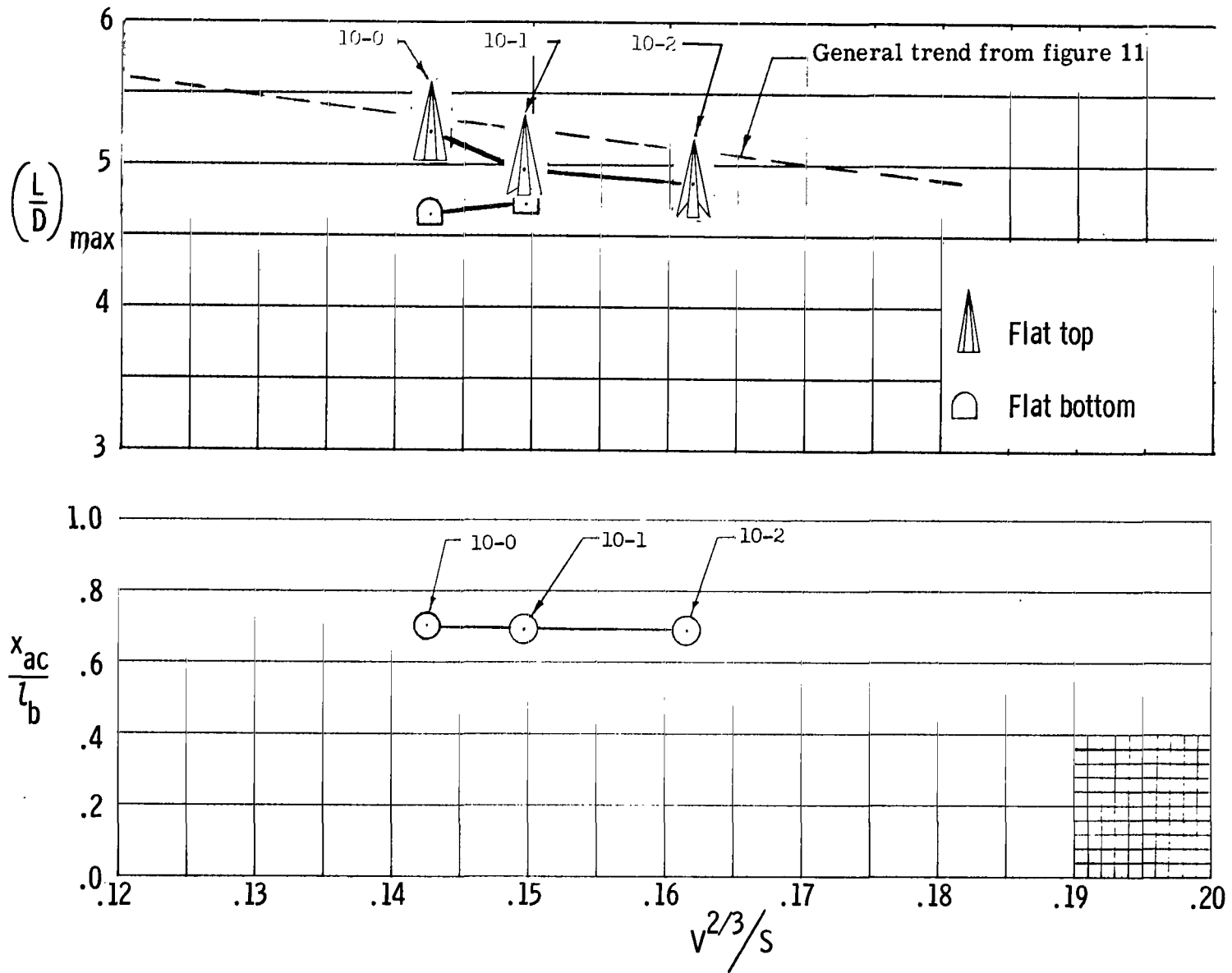


Figure 9.- Effect on  $(L/D)_{max}$  and aerodynamic-center location of reducing wing-root area of models with delta wings.  $R = 1.5 \times 10^6$ ,  $M = 6.8$ .

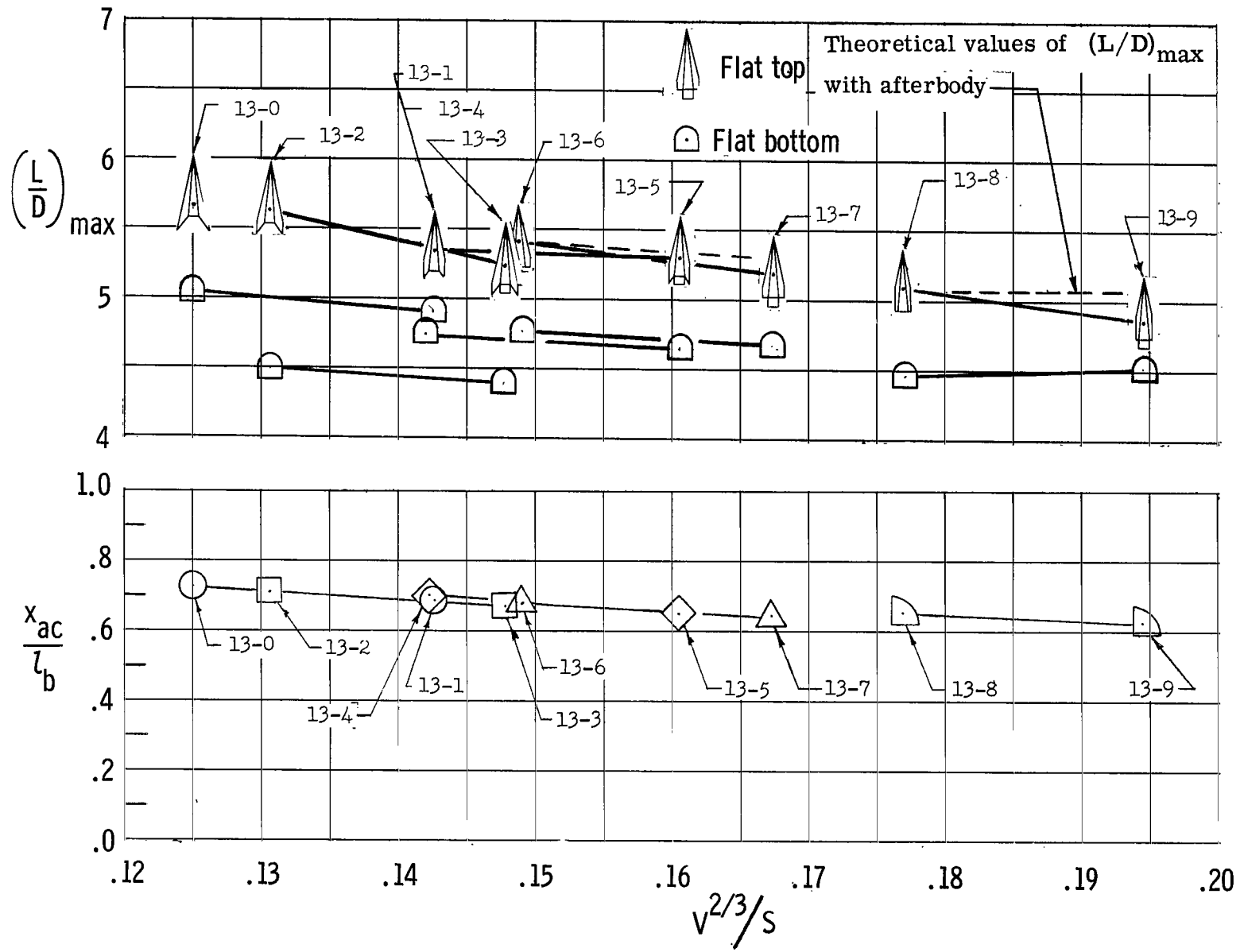


Figure 10.- Effect on  $(L/D)_{\max}$  and aerodynamic-center location of addition of afterbodies on various models.  $R = 1.5 \times 10^6$ ;  $M = 6.8$ .

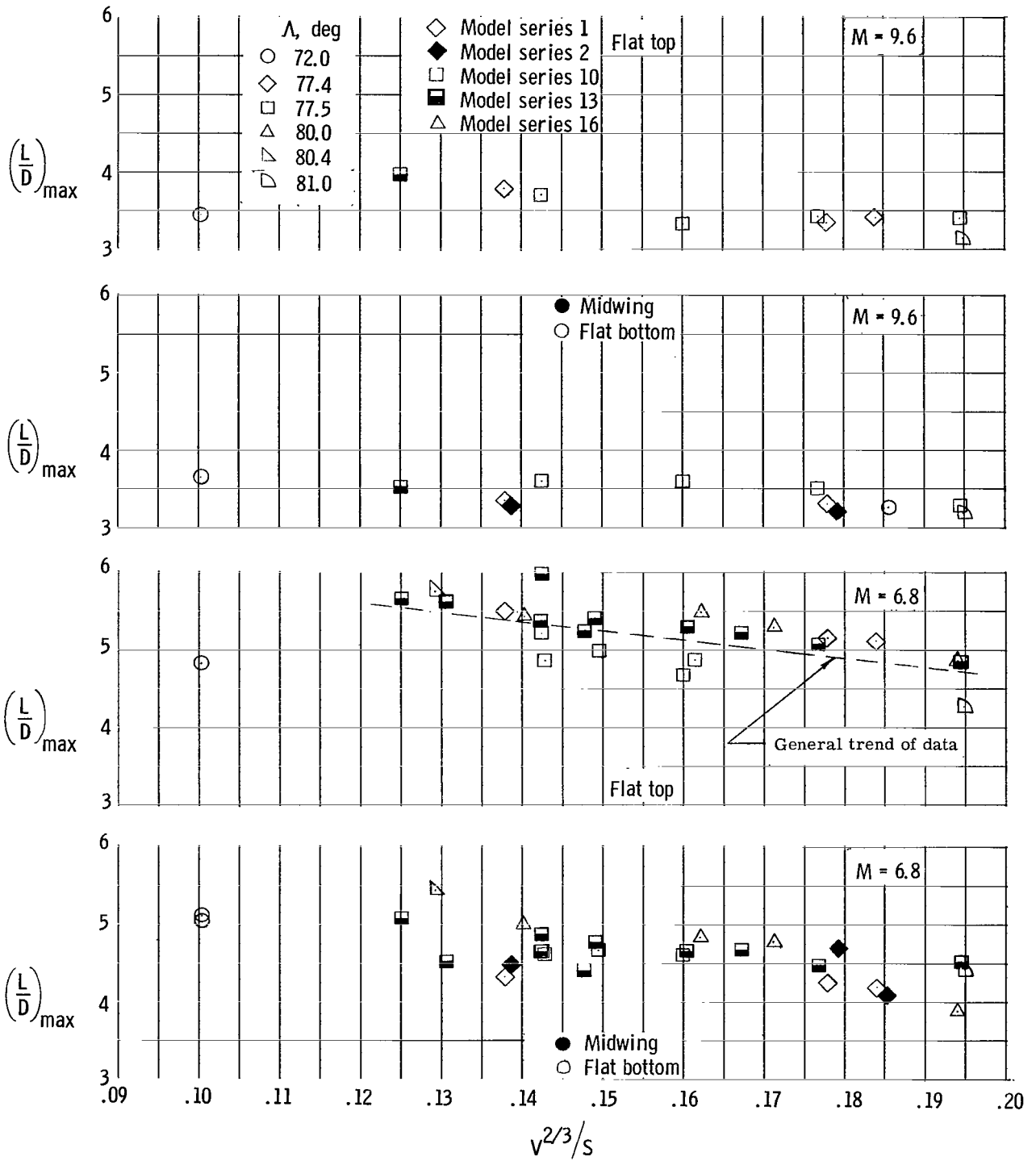


Figure 11.- Variation of maximum lift-drag ratio with volume parameter.  $M = 9.6$ ,  $R \approx 0.7 \times 10^6$ ;  $M = 6.8$ ,  $R \approx 1.5 \times 10^6$ .

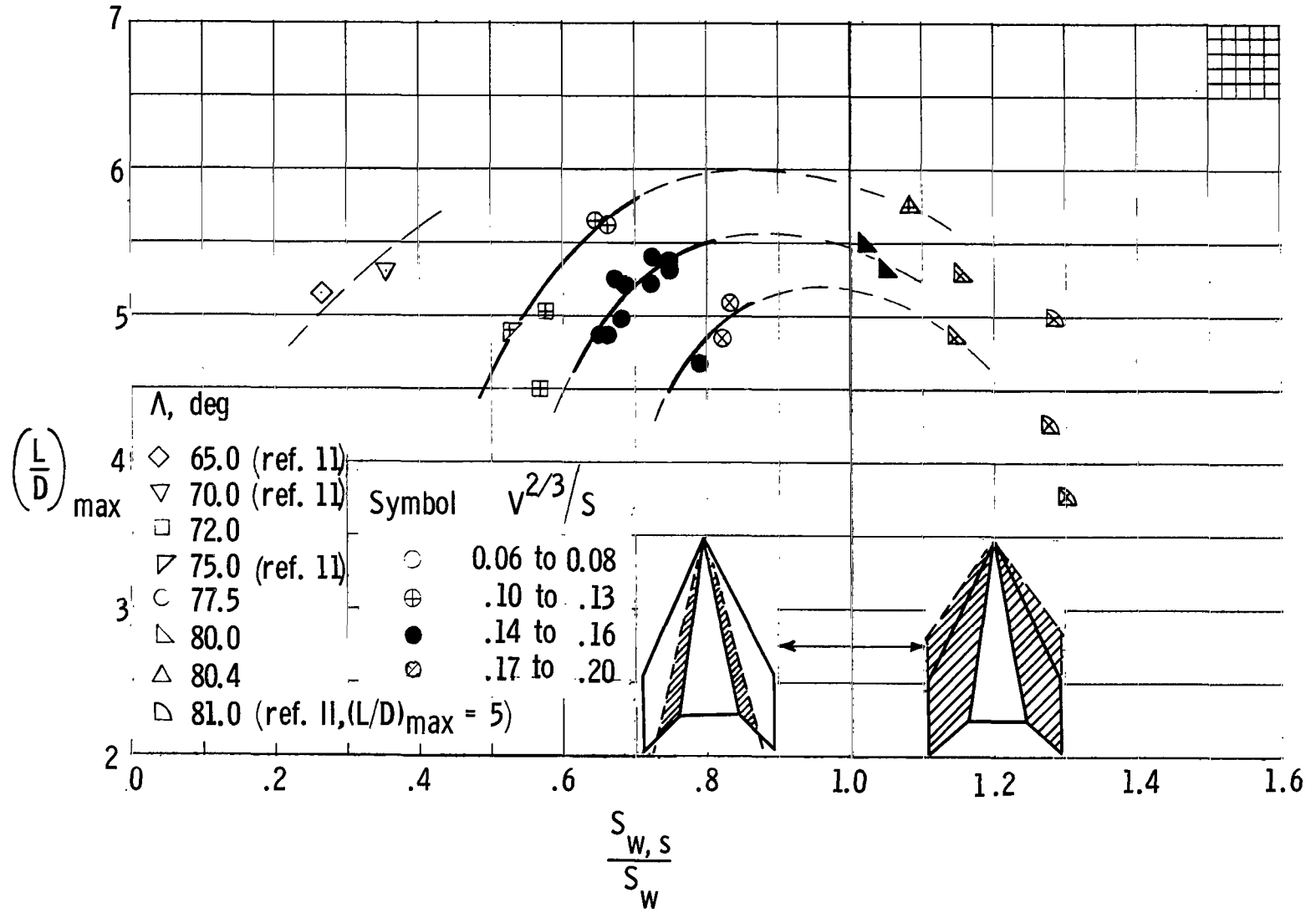
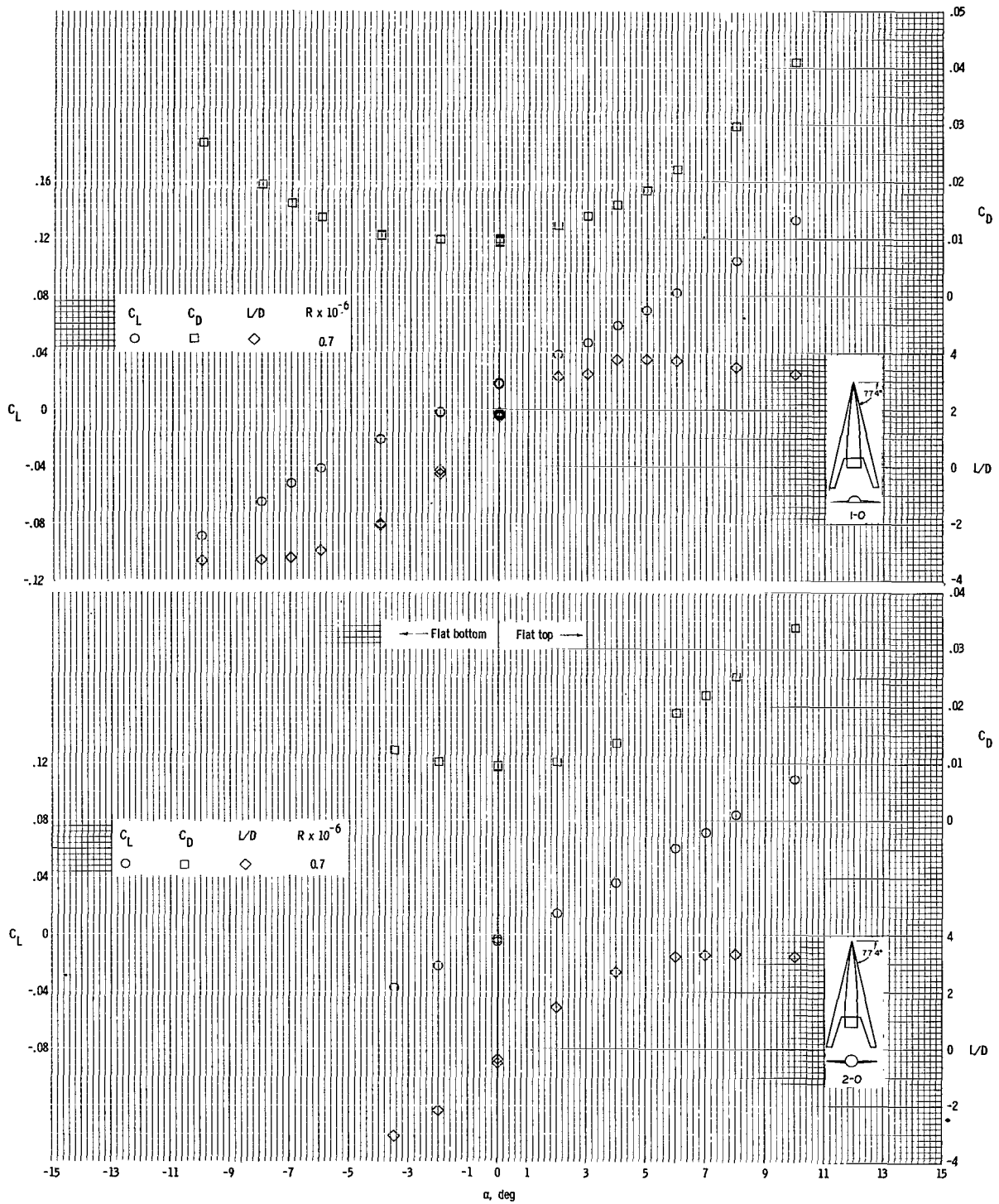
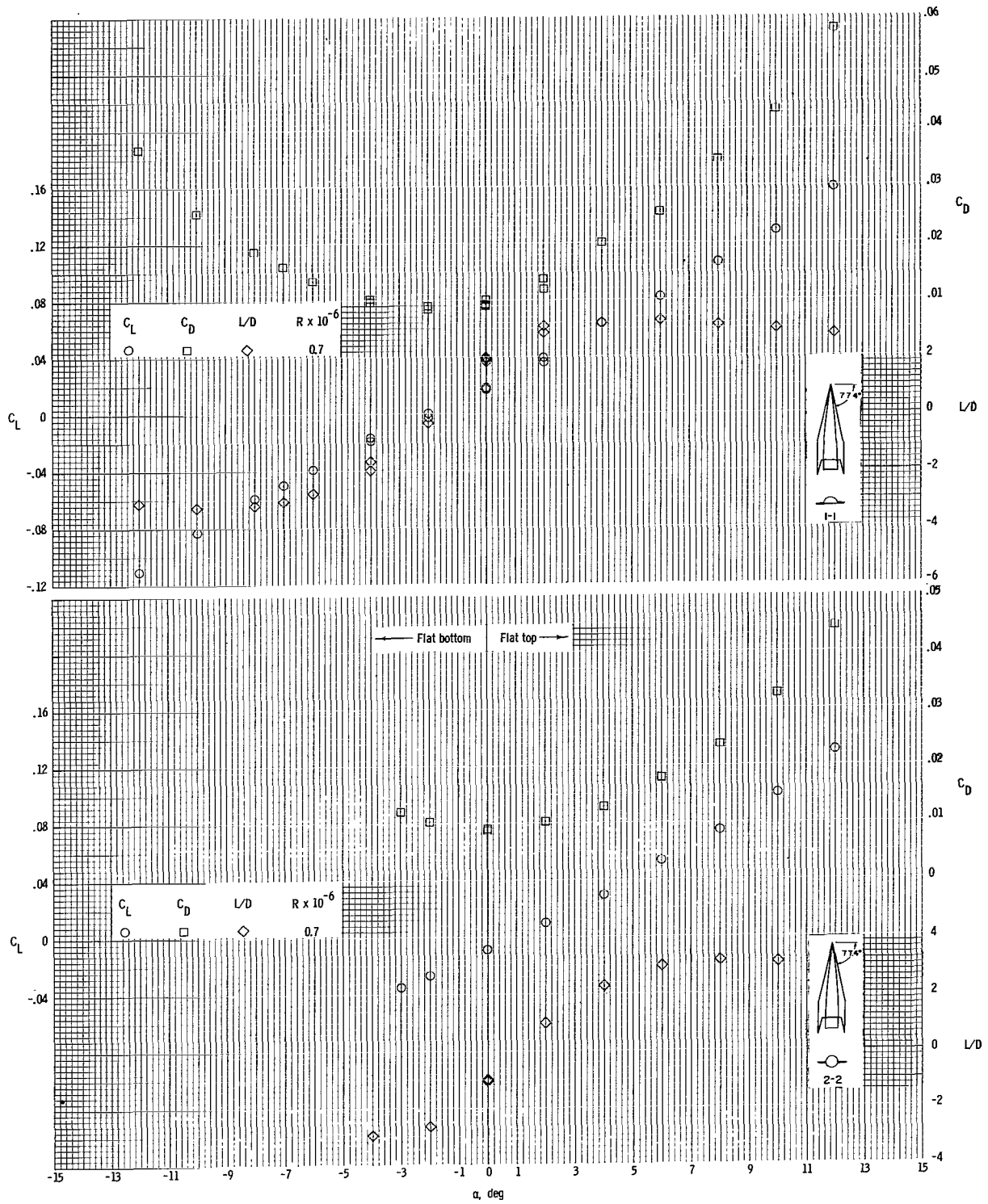


Figure 12.- Wing-planform correlation for flat-top configurations.  $R = 1.5 \times 10^6$ ;  $M = 6.8$ .



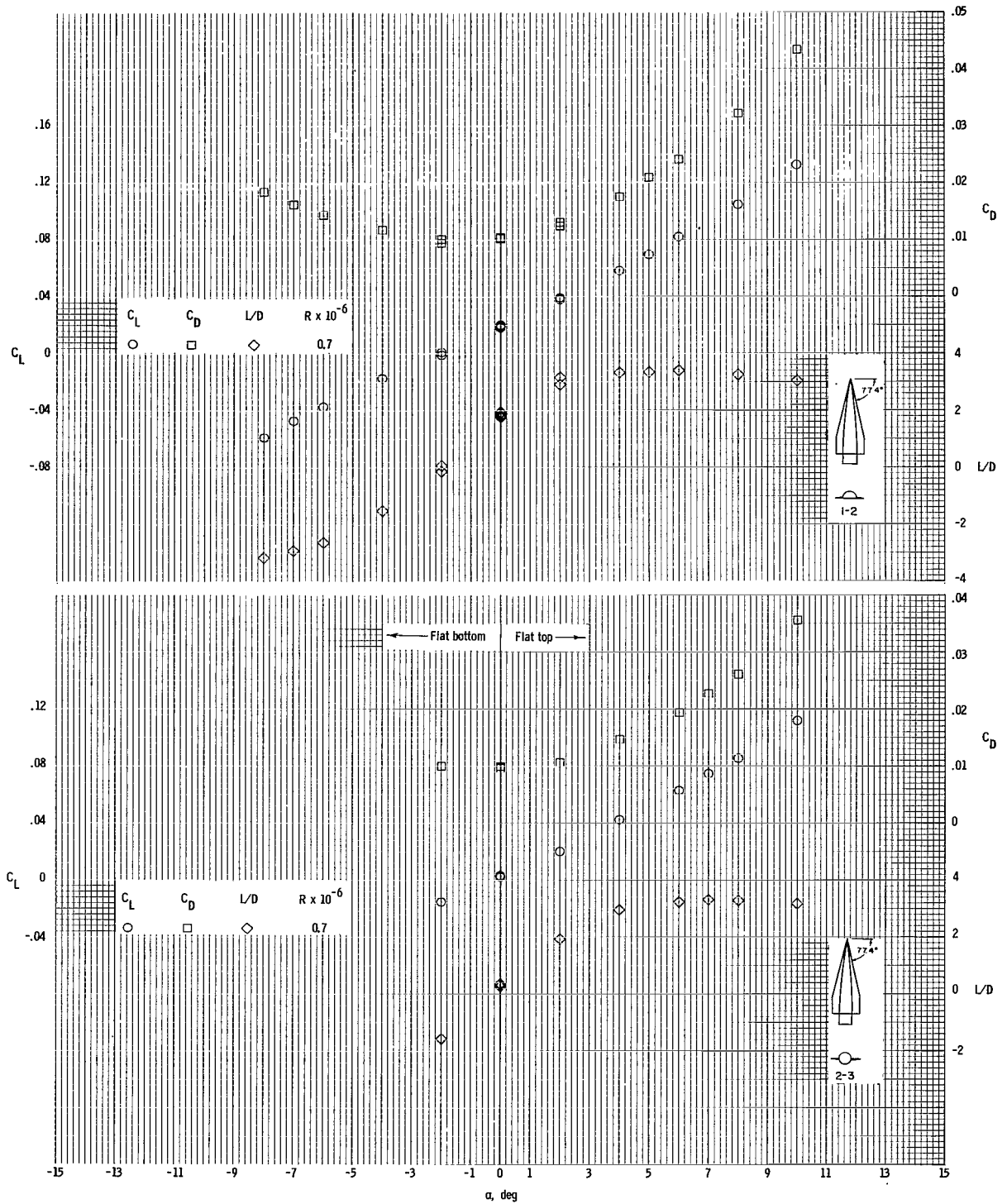
(a) Models 1-0 and 2-0.

Figure 13.- Lift coefficient, drag coefficient, and lift-drag ratio as a function of angle of attack at  $M = 9.6$ .



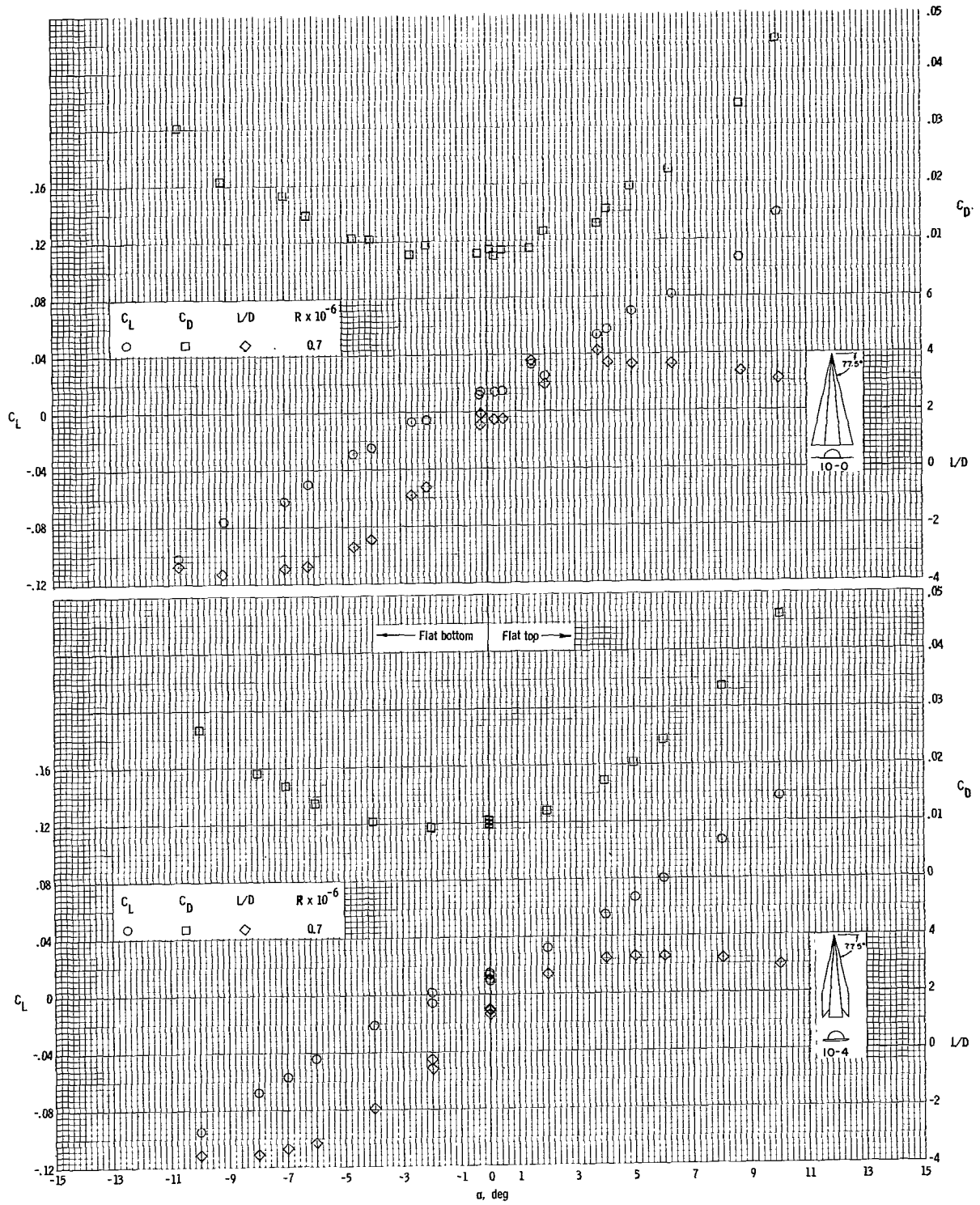
(b) Models 1-1 and 2-2.

Figure 13.- Continued.



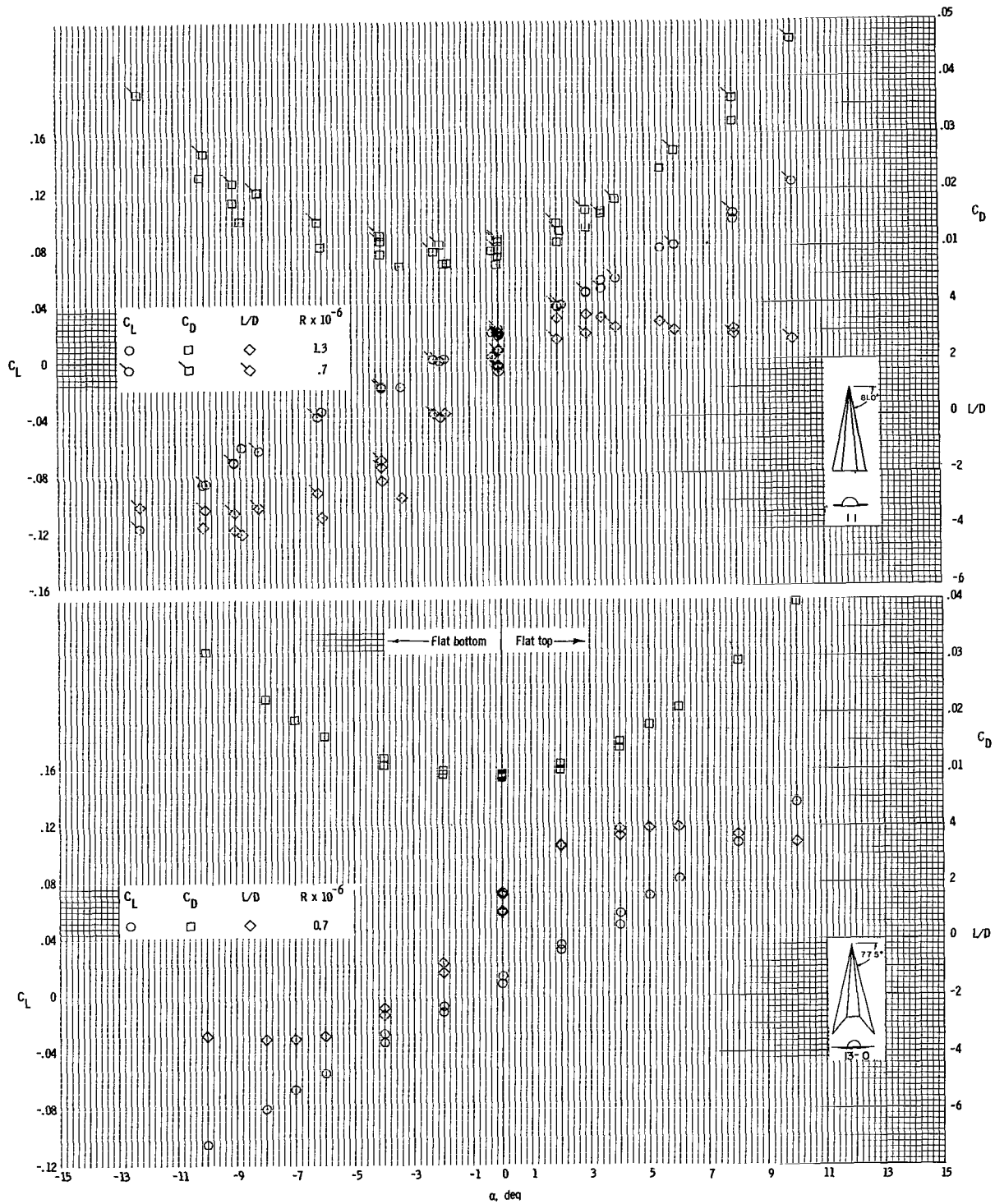
(c) Models 1-2 and 2-3.

Figure 13.- Continued.



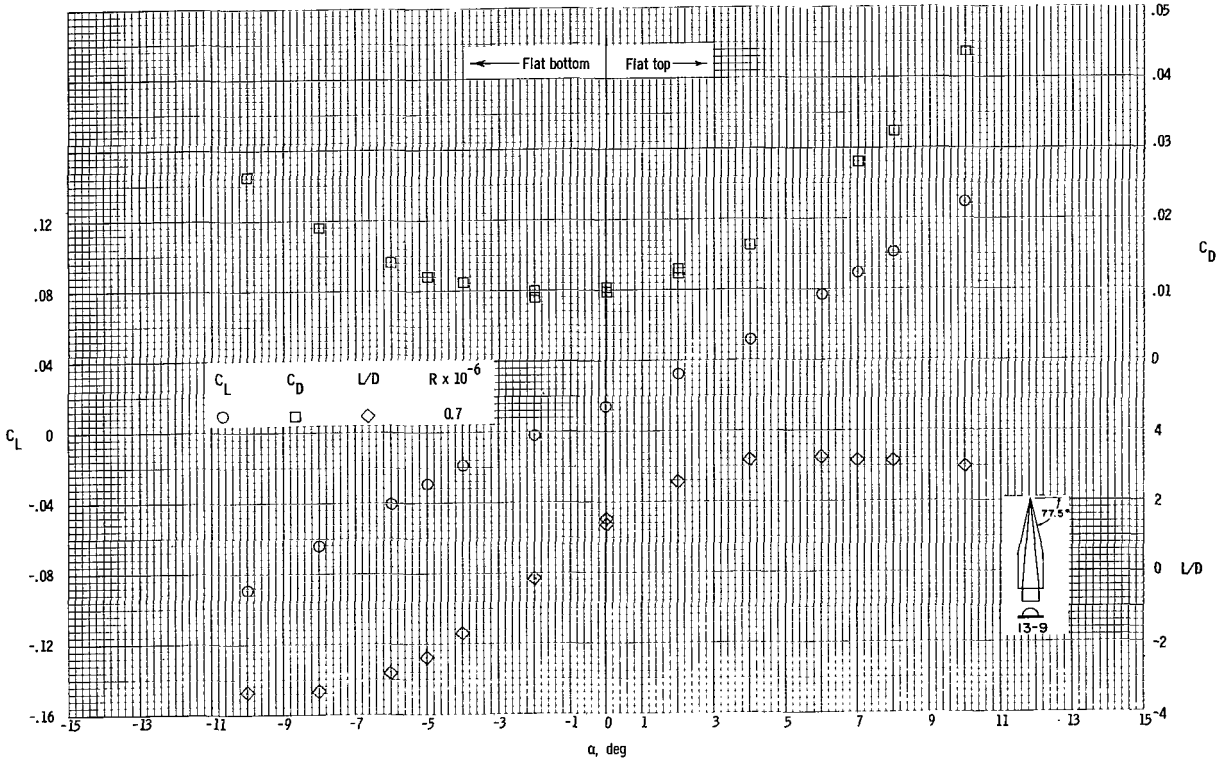
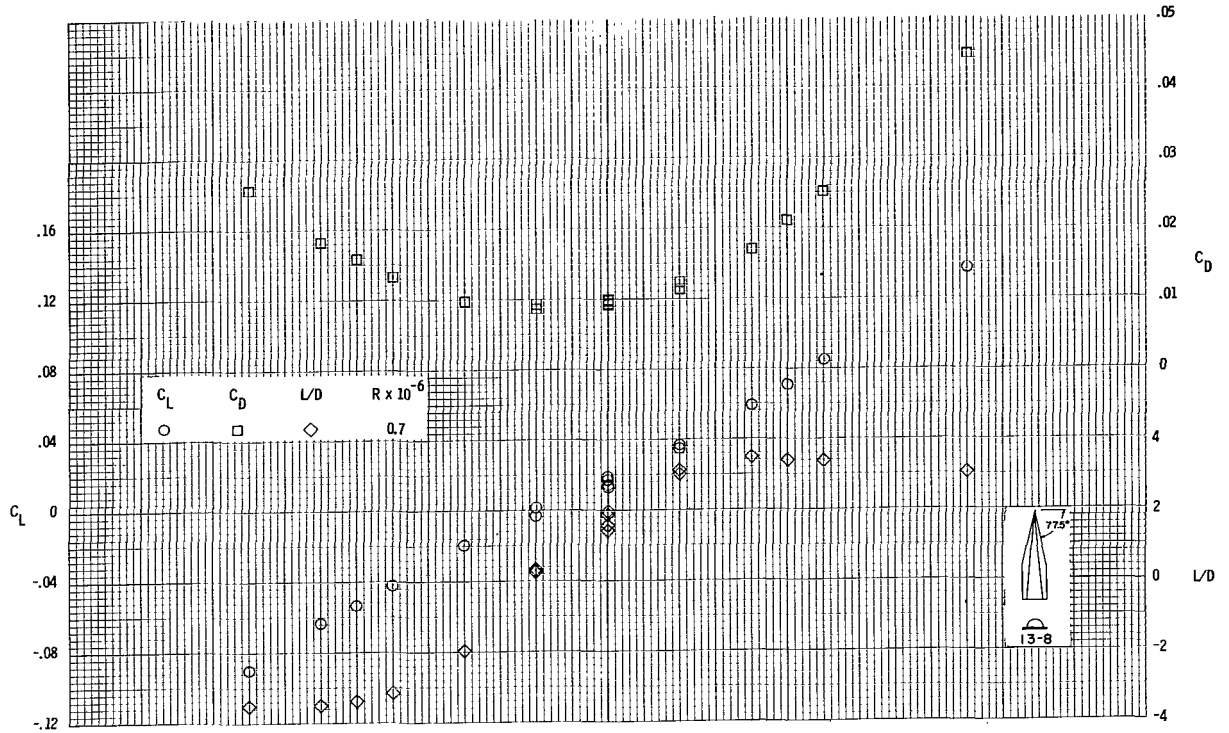
(d) Models 10-0 and 10-4.

Figure 13.- Continued.



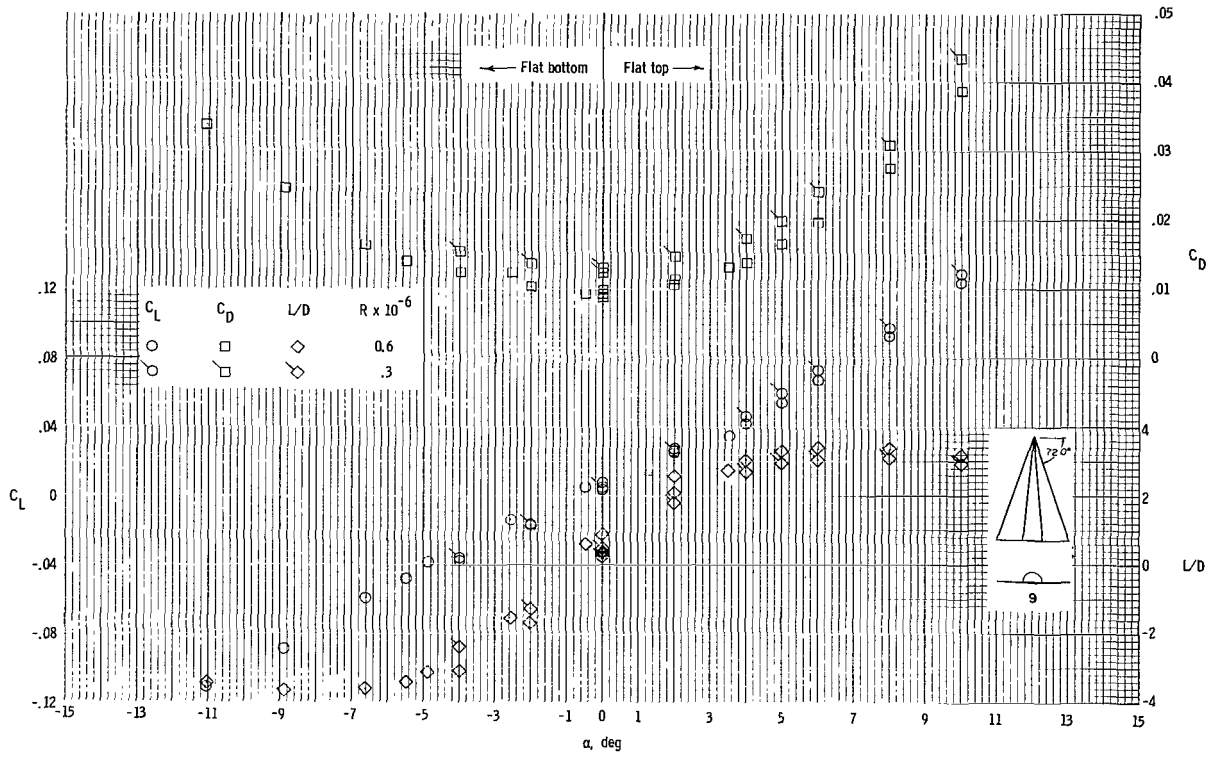
(e) Models 11 and 13-0.

Figure 13.- Continued.



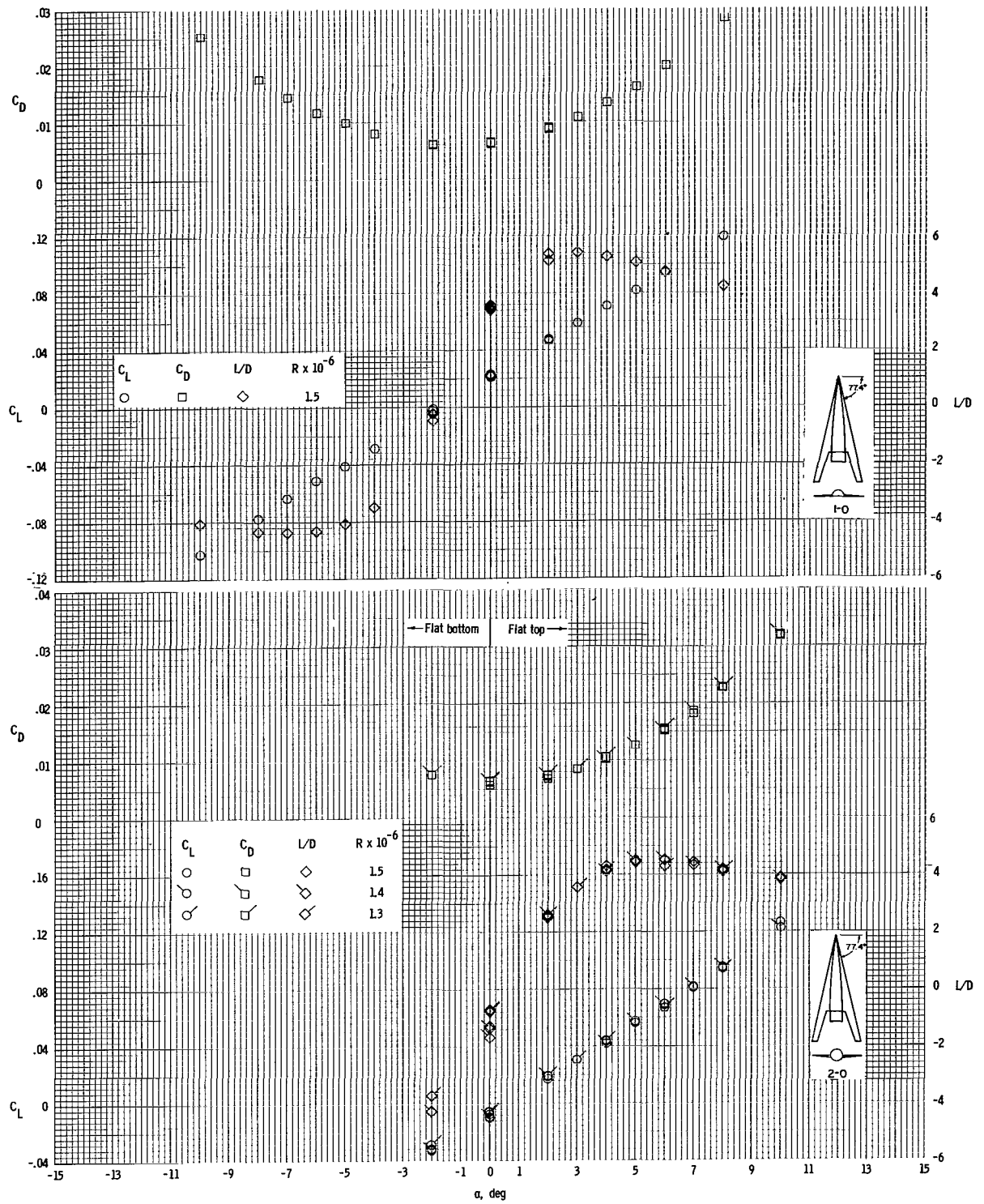
(f) Models 13-8 and 13-9.

Figure 13.- Continued.



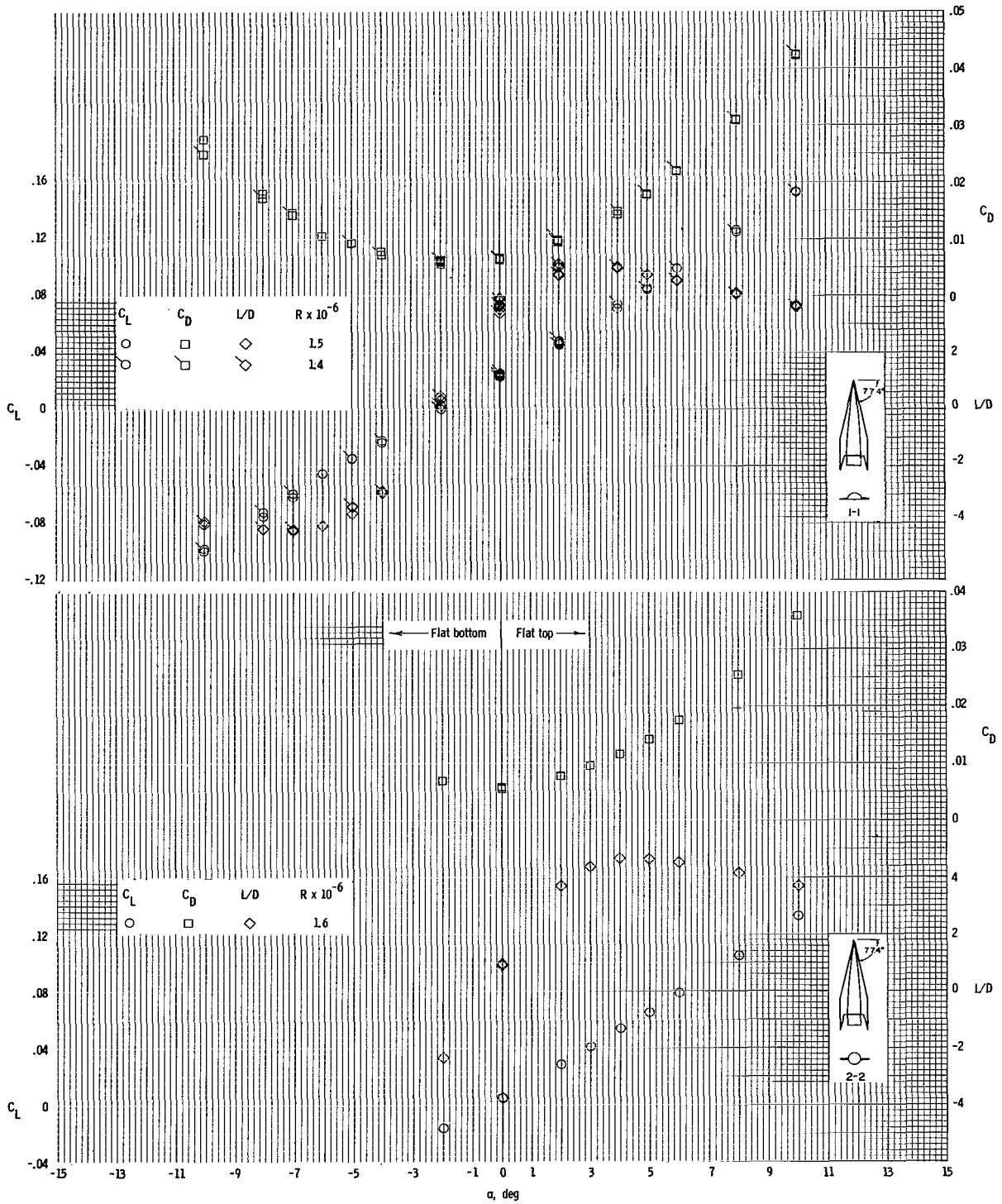
(g) Model 9.

Figure 13.- Concluded.



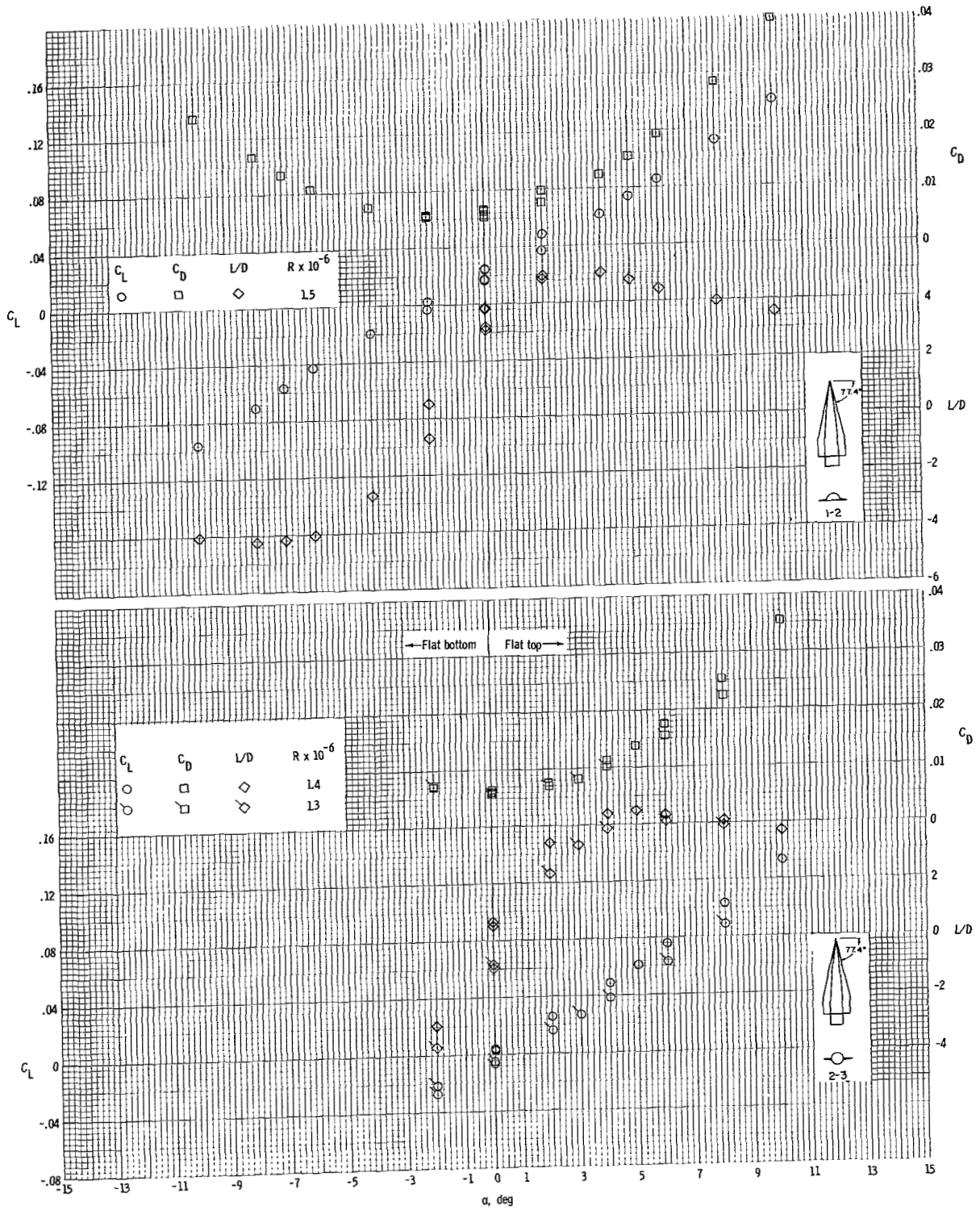
(a) Models 1-0 and 2-0.

Figure 14.- Lift coefficient, drag coefficient, and lift-drag ratio as a function of angle of attack at  $M = 6.8$ .



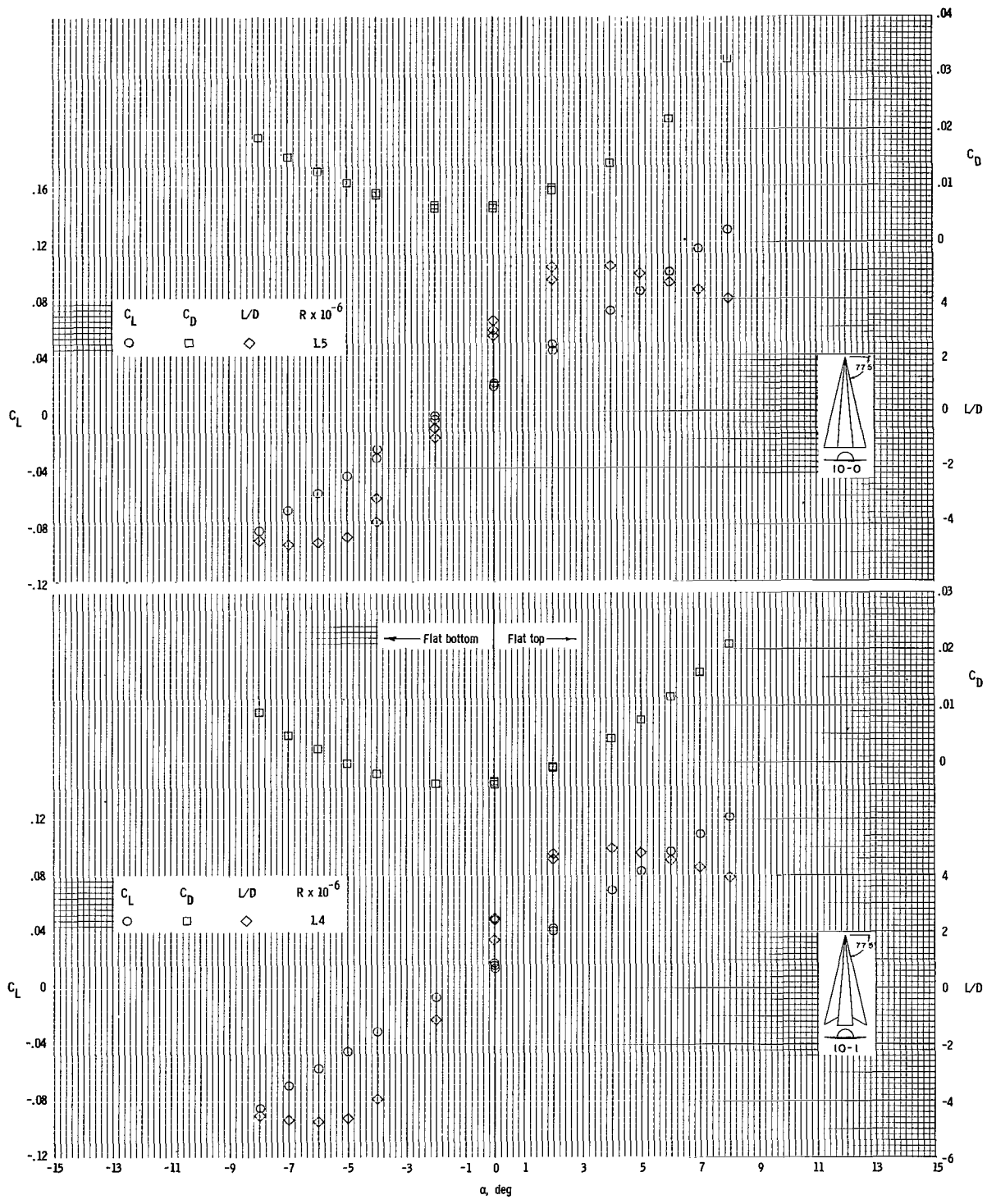
(b) Models 1-1 and 2-2.

Figure 14.- Continued.



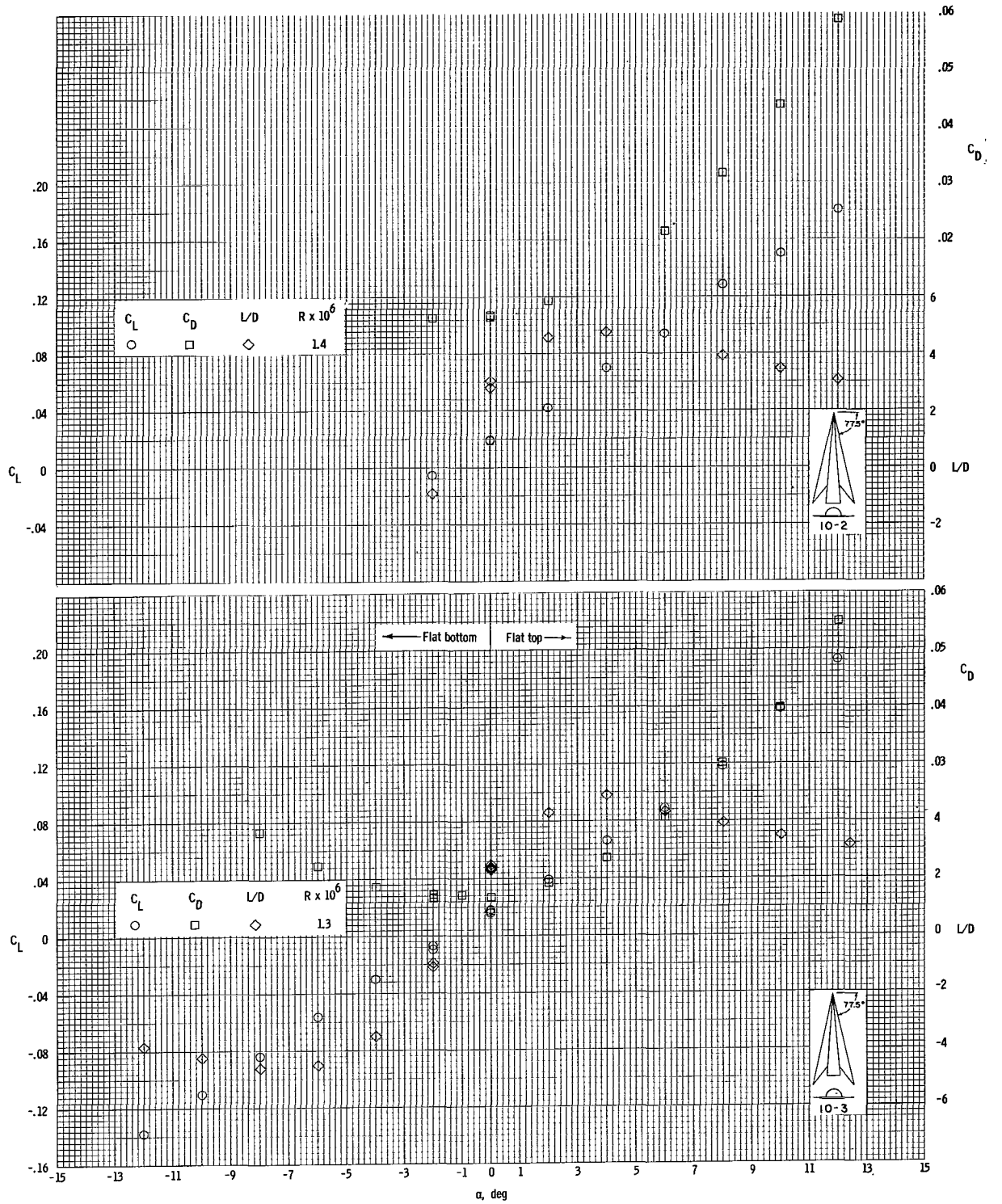
(c) Models 1-2 and 2-3.

Figure 14.- Continued.



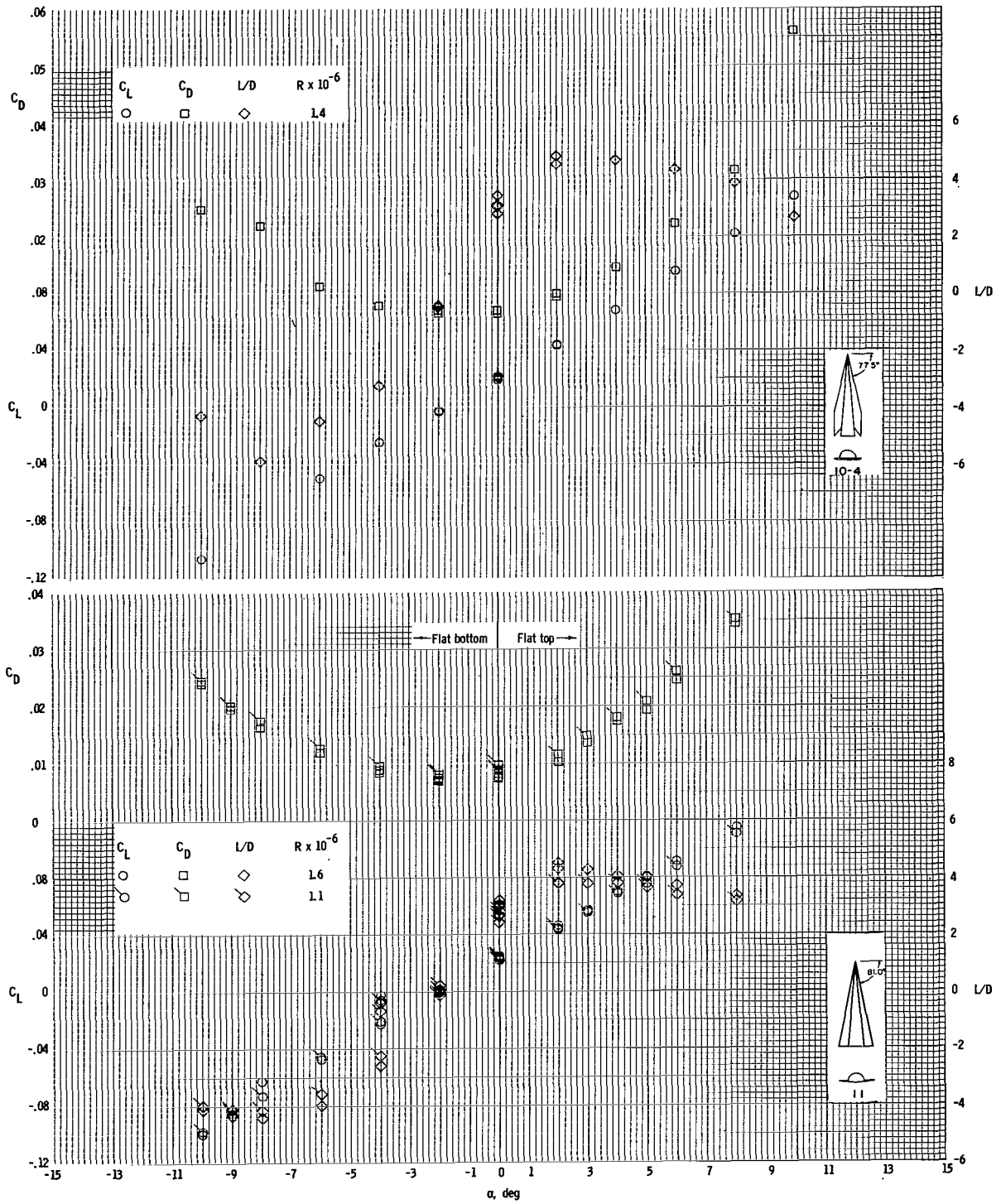
(d) Models 10-0 and 10-1.

Figure 14.- Continued.



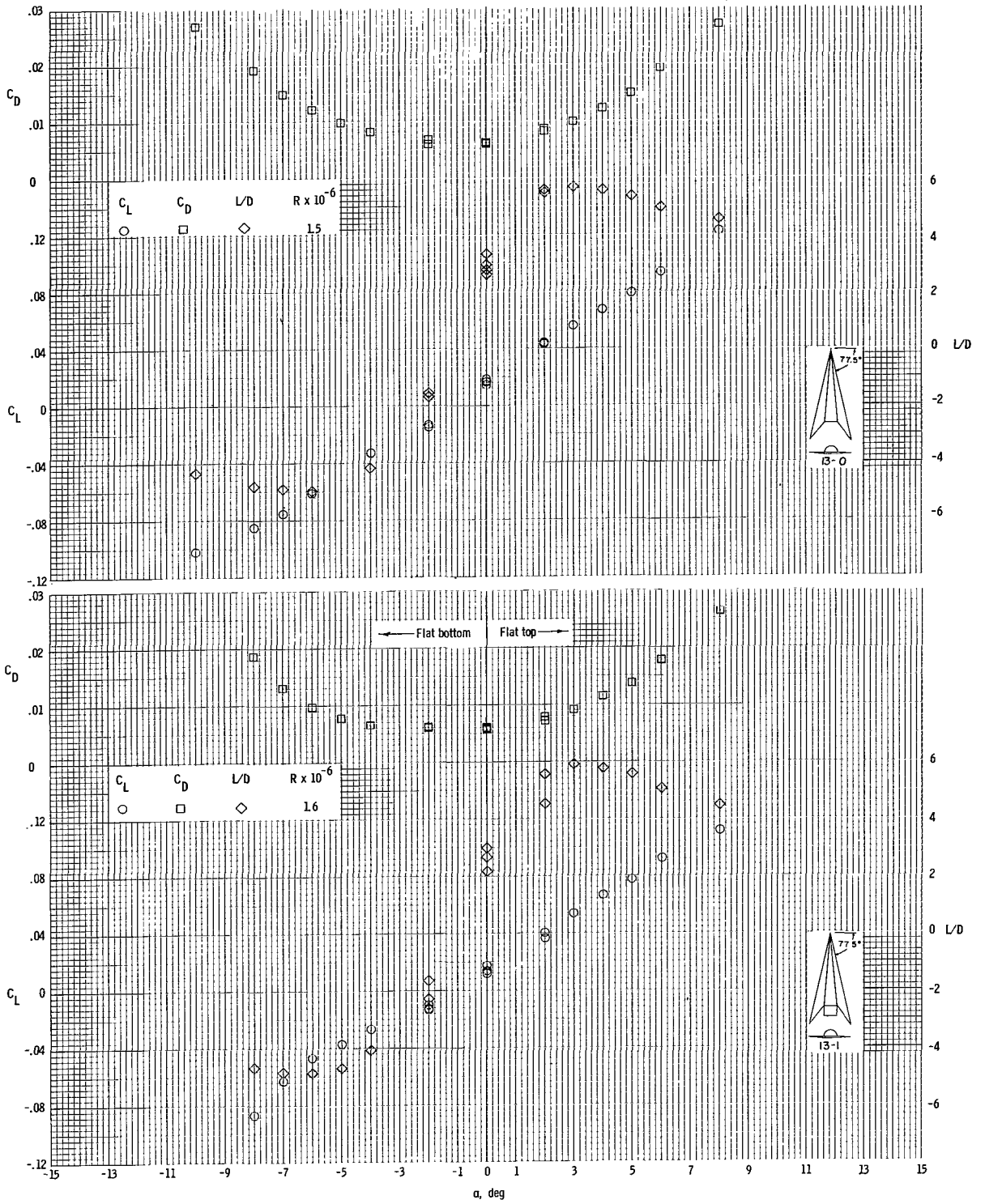
(e) Models 10-2 and 10-3.

Figure 14.- Continued.



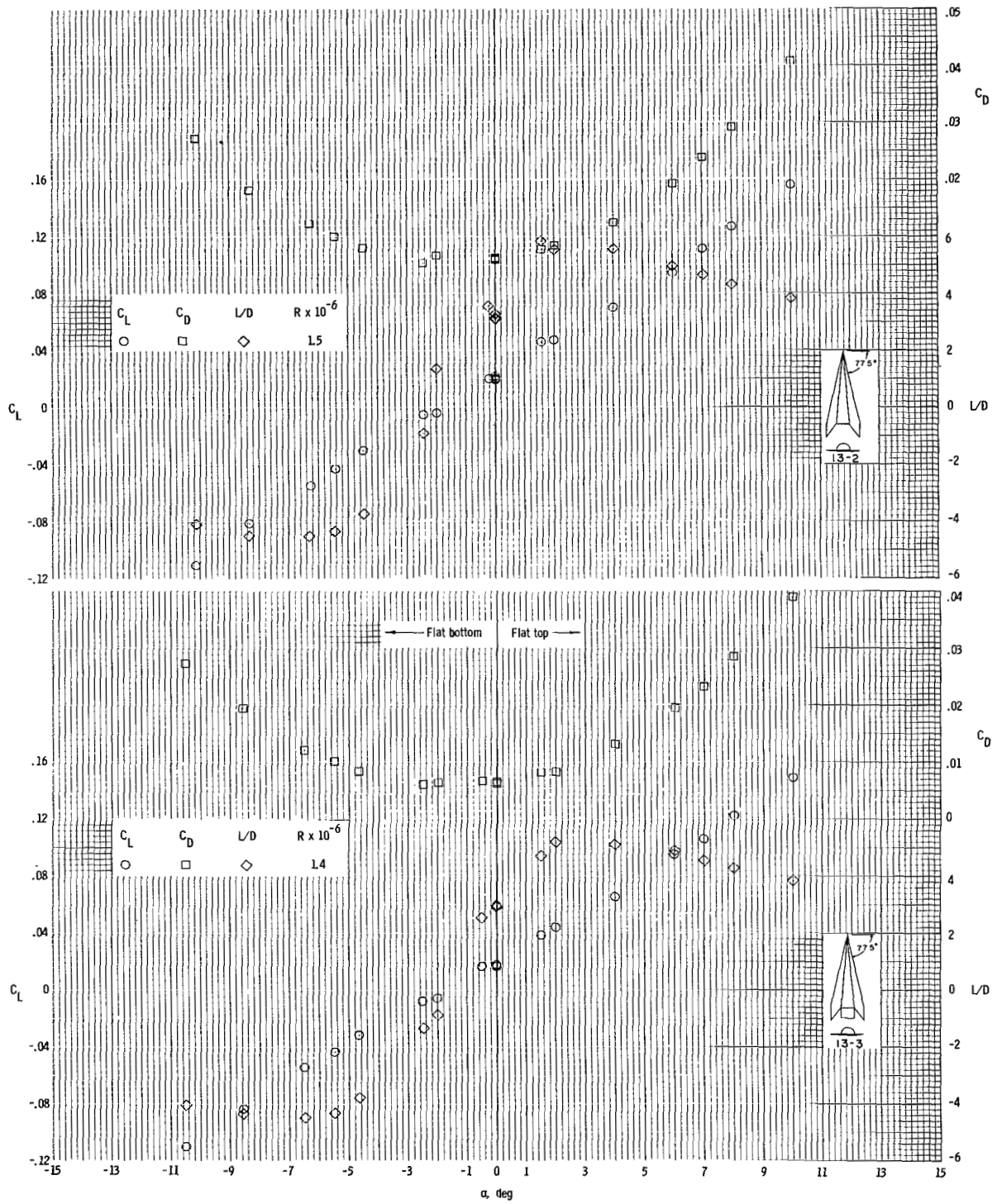
(f) Models 10-4 and 11.

Figure 14.- Continued.



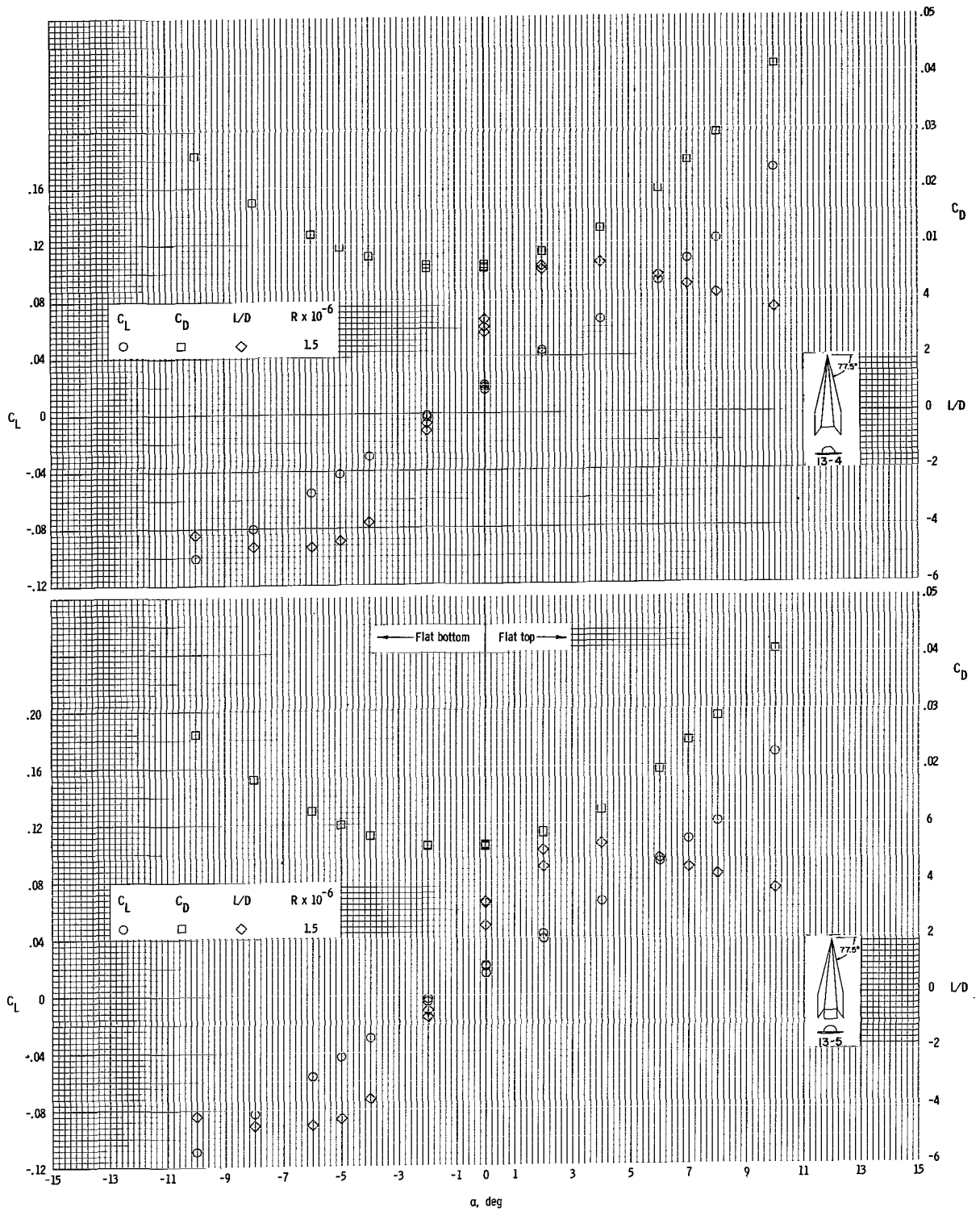
(g) Models 13-0 and 13-1.

Figure 14.- Continued.



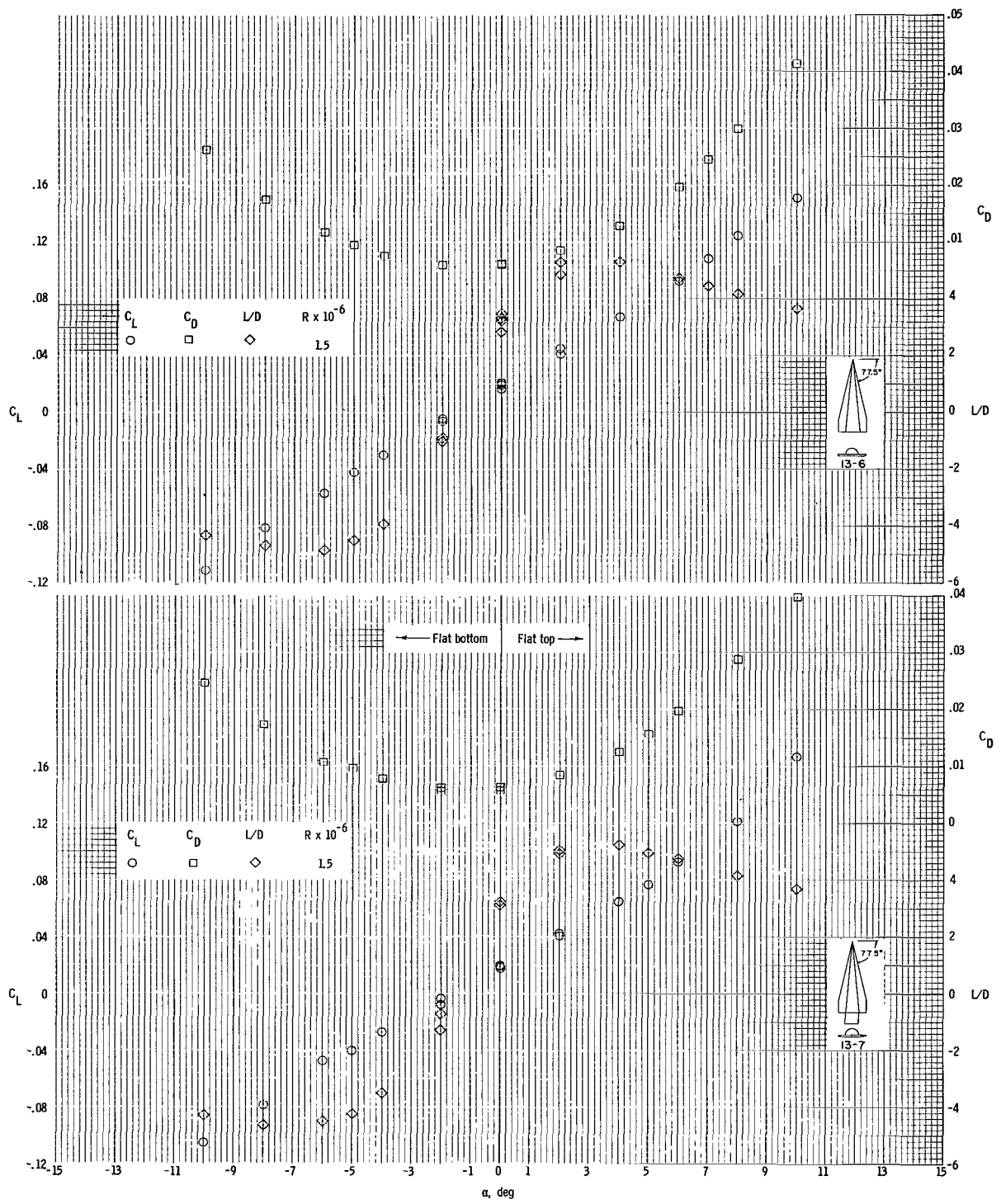
(h) Models 13-2 and 13-3.

Figure 14.- Continued.



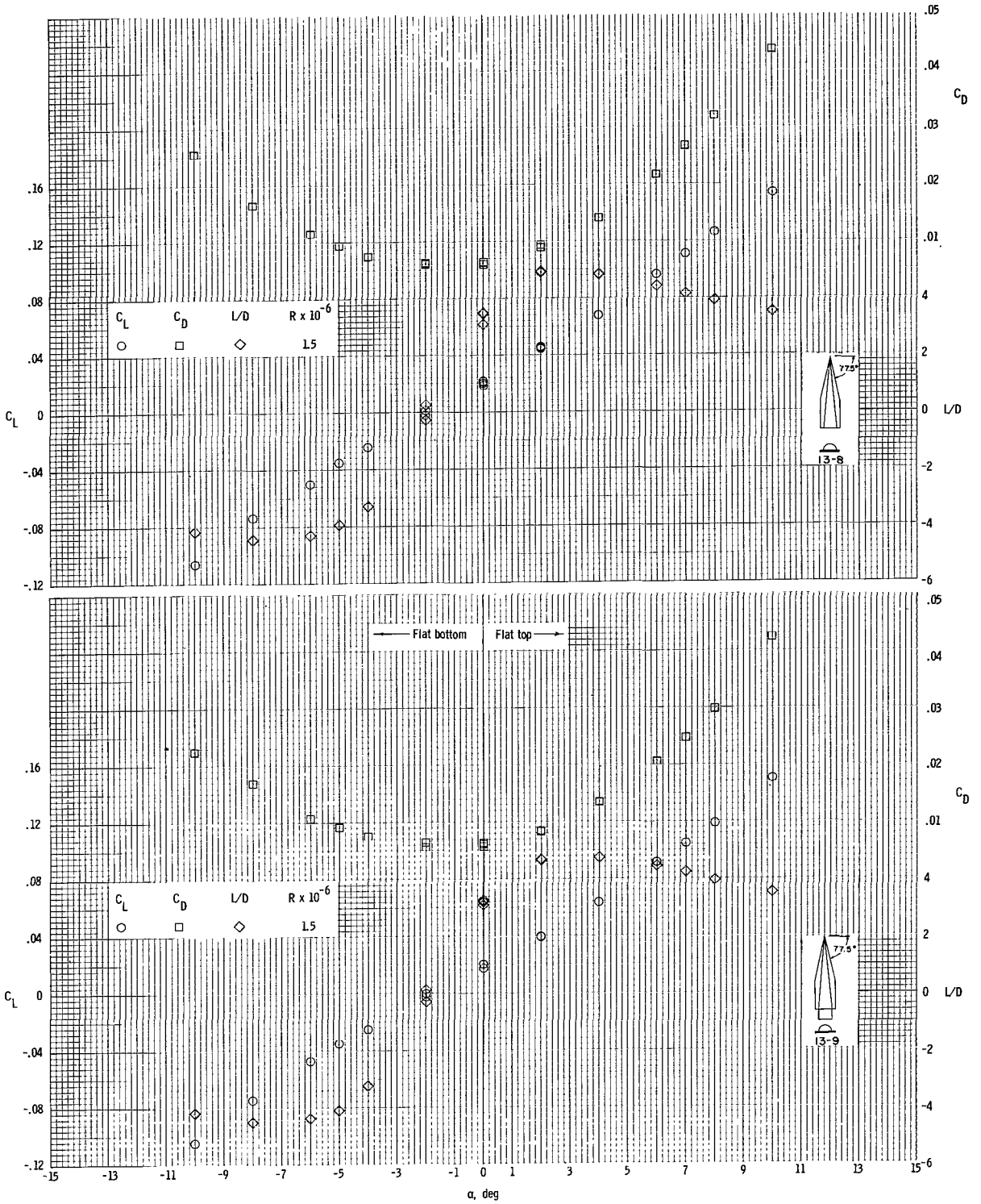
(i) Models 13-4 and 13-5.

Figure 14.- Continued.



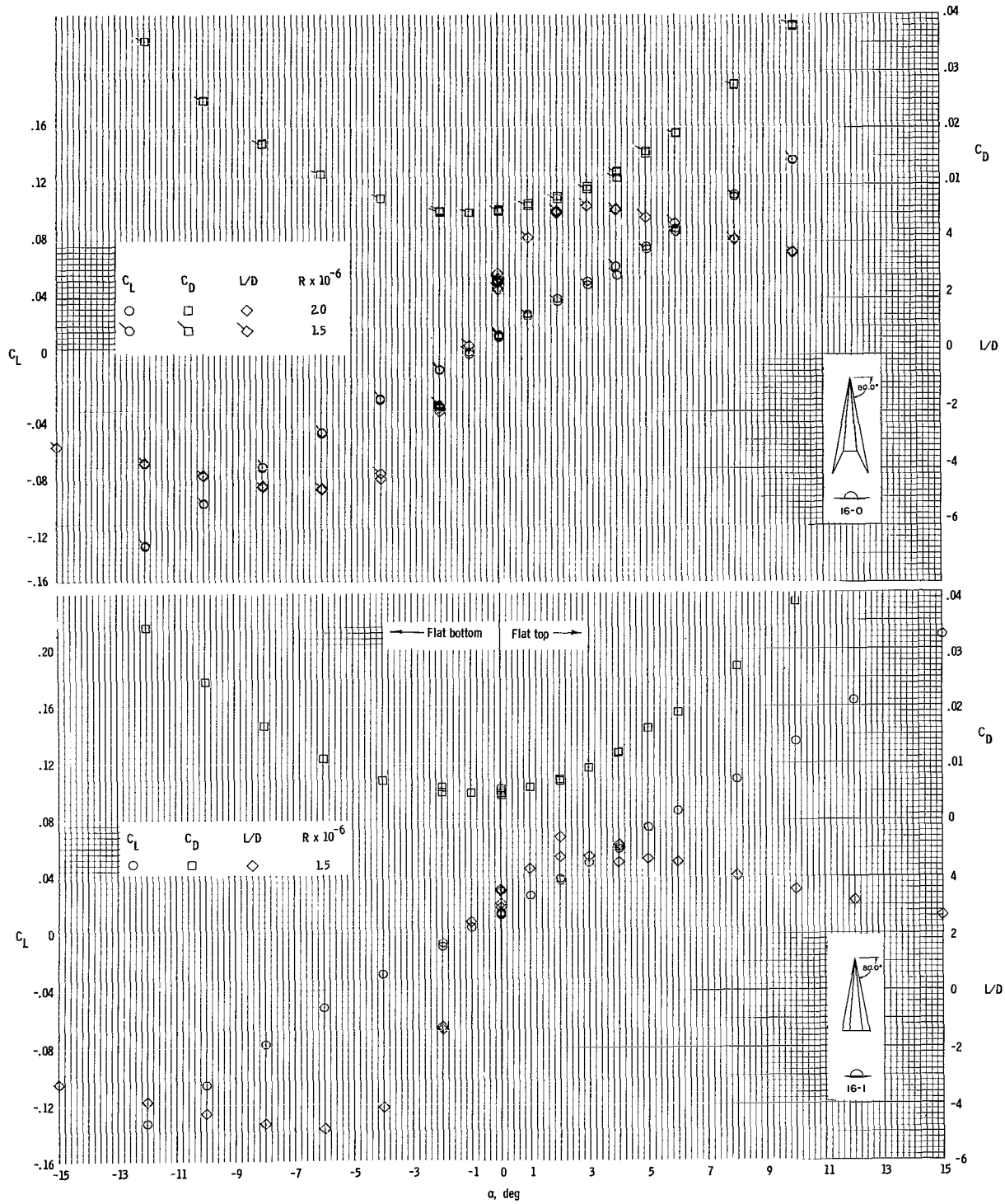
(j) Models 13-6 and 13-7.

Figure 14.- Continued.



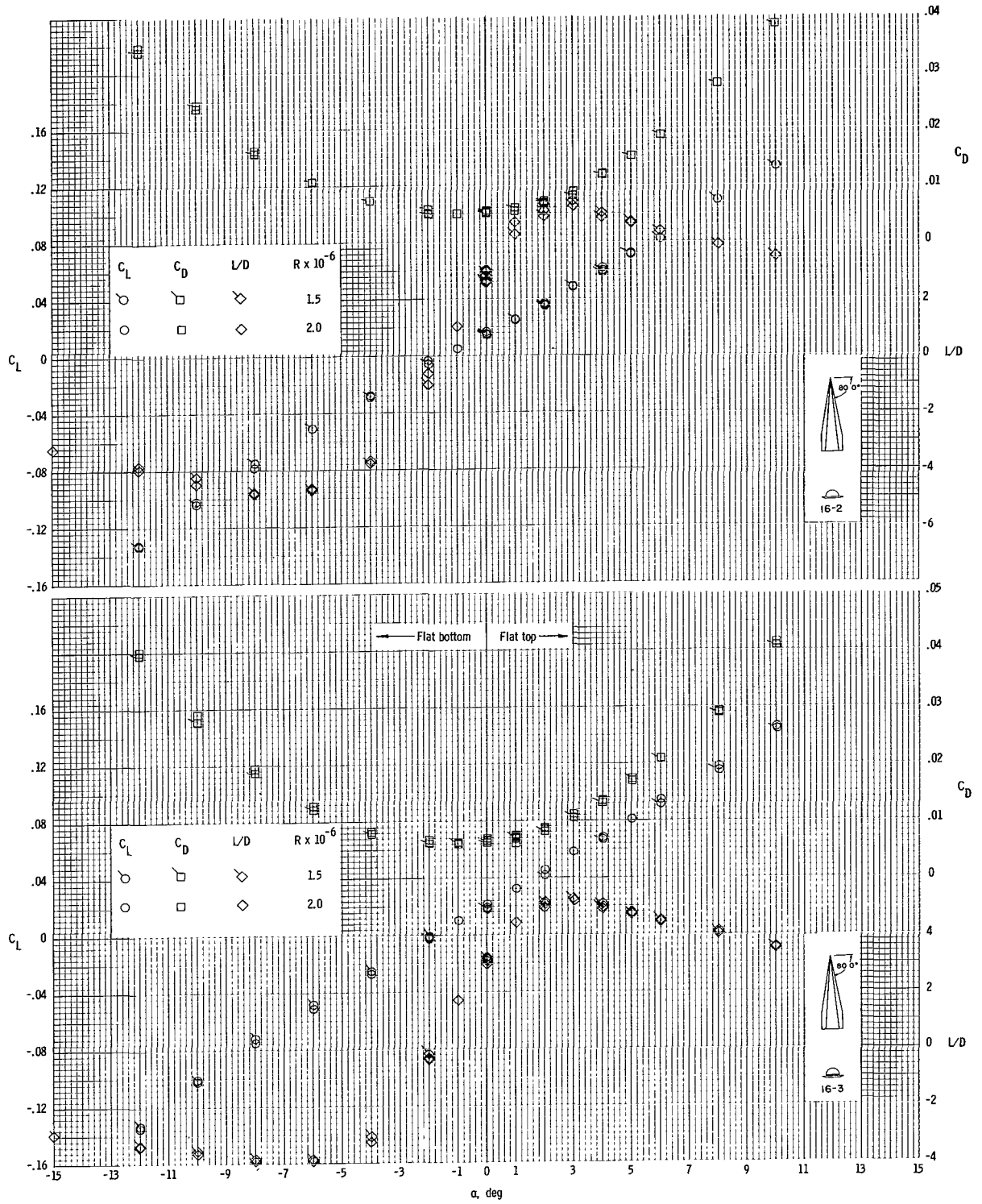
(k) Models 13-8 and 13-9.

Figure 14.- Continued.



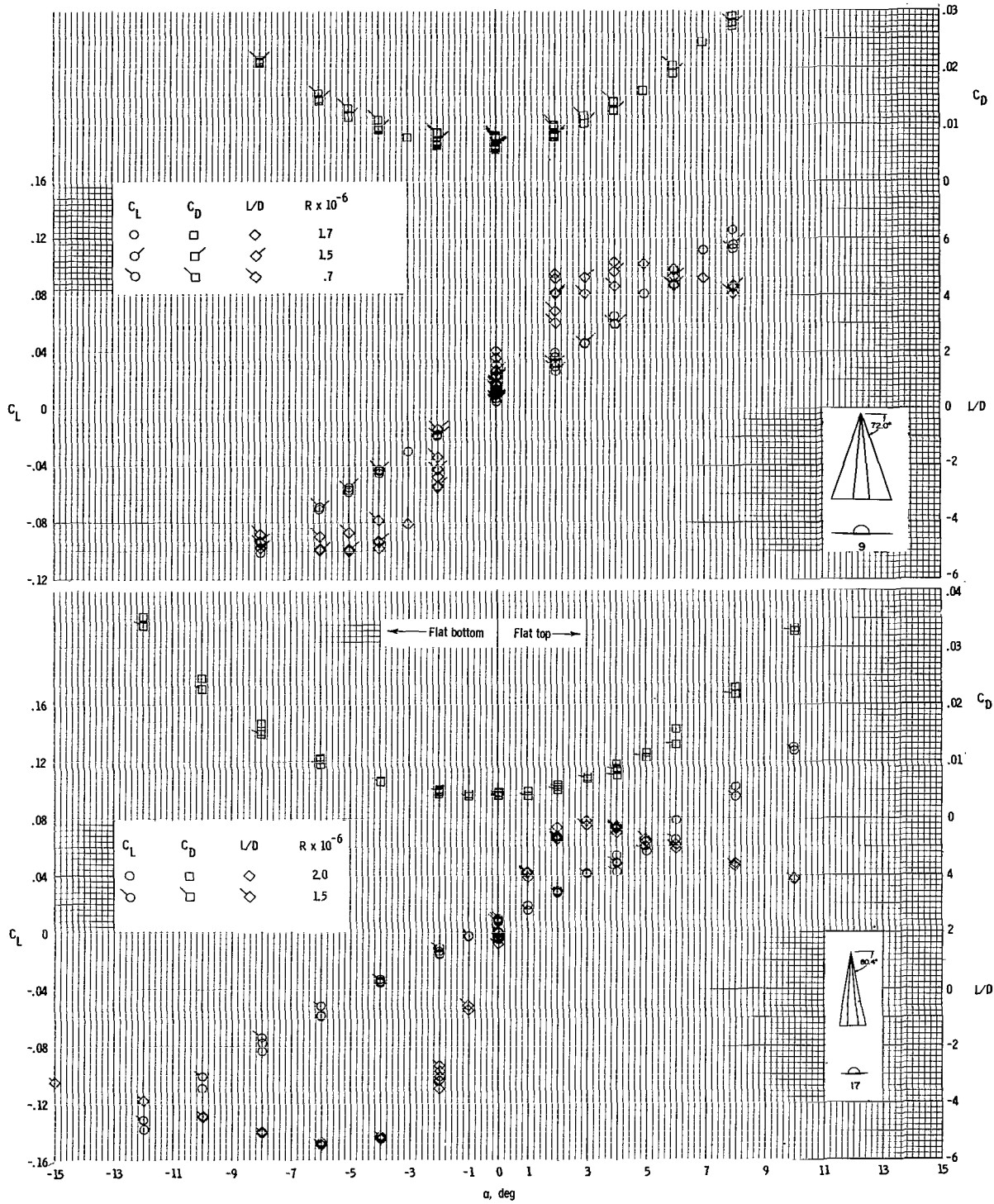
(I) Models 16-0 and 16-1.

Figure 14.- Continued.



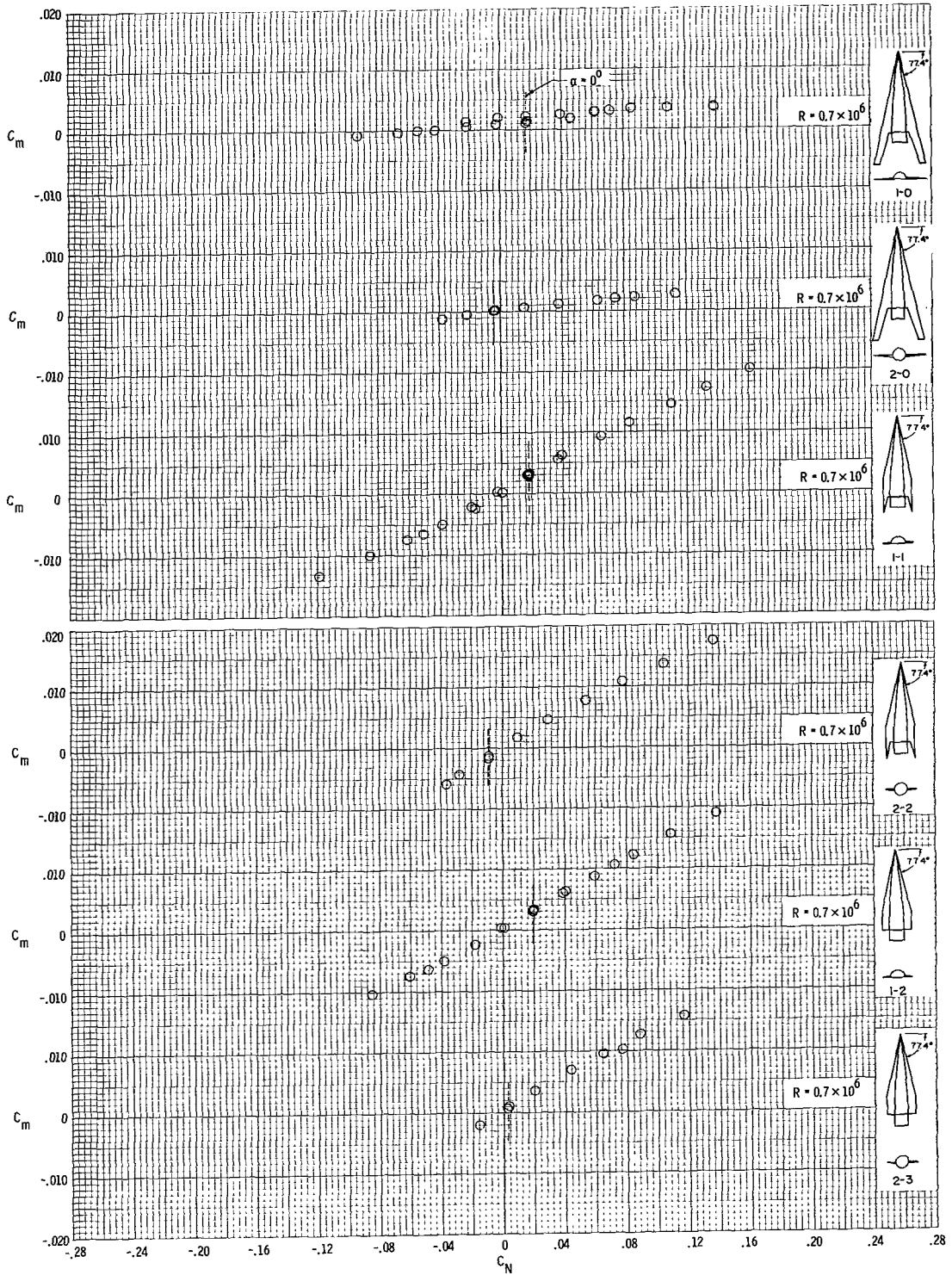
(m) Models 16-2 and 16-3.

Figure 14.- Continued.



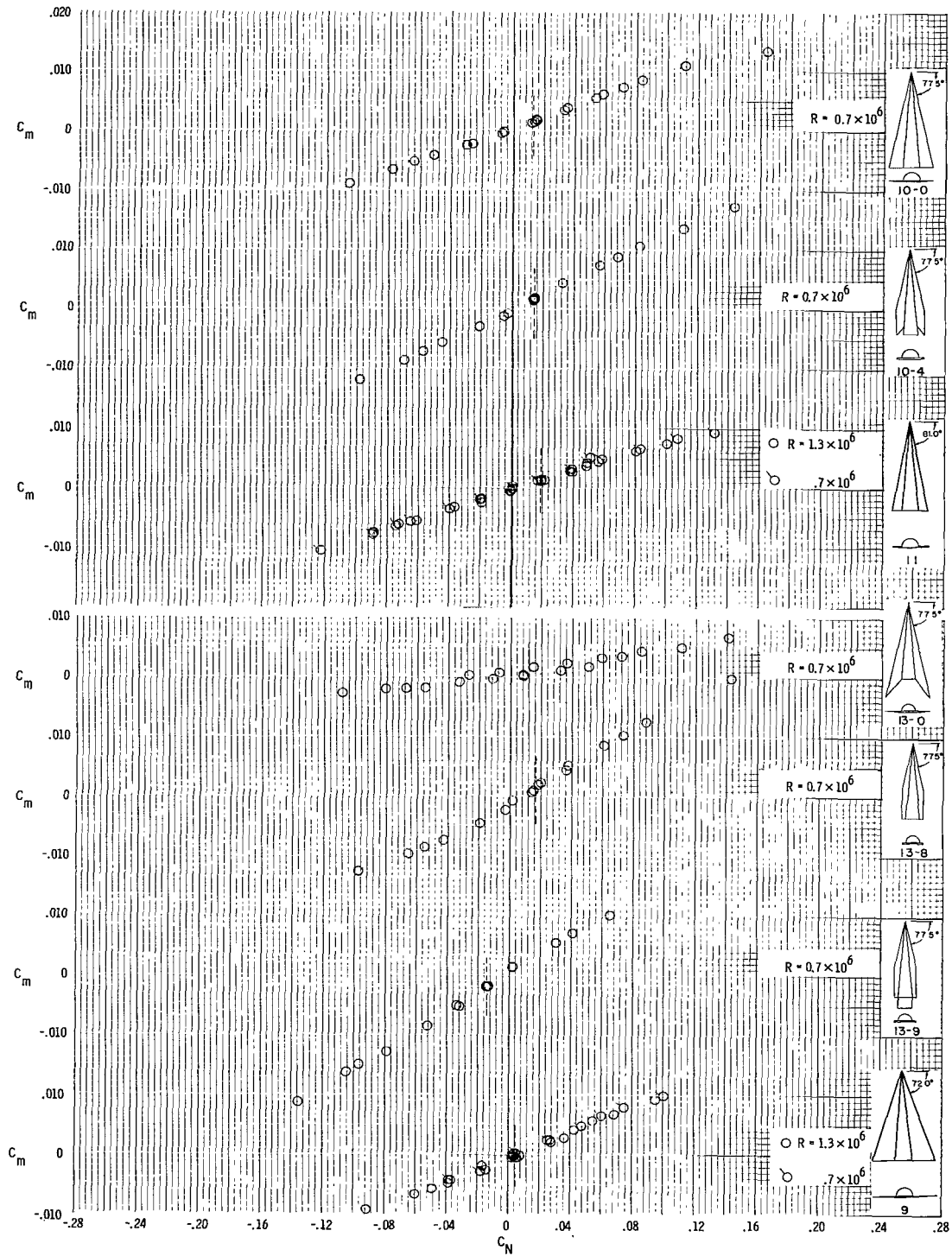
(n) Models 9 and 17.

Figure 14.- Concluded.



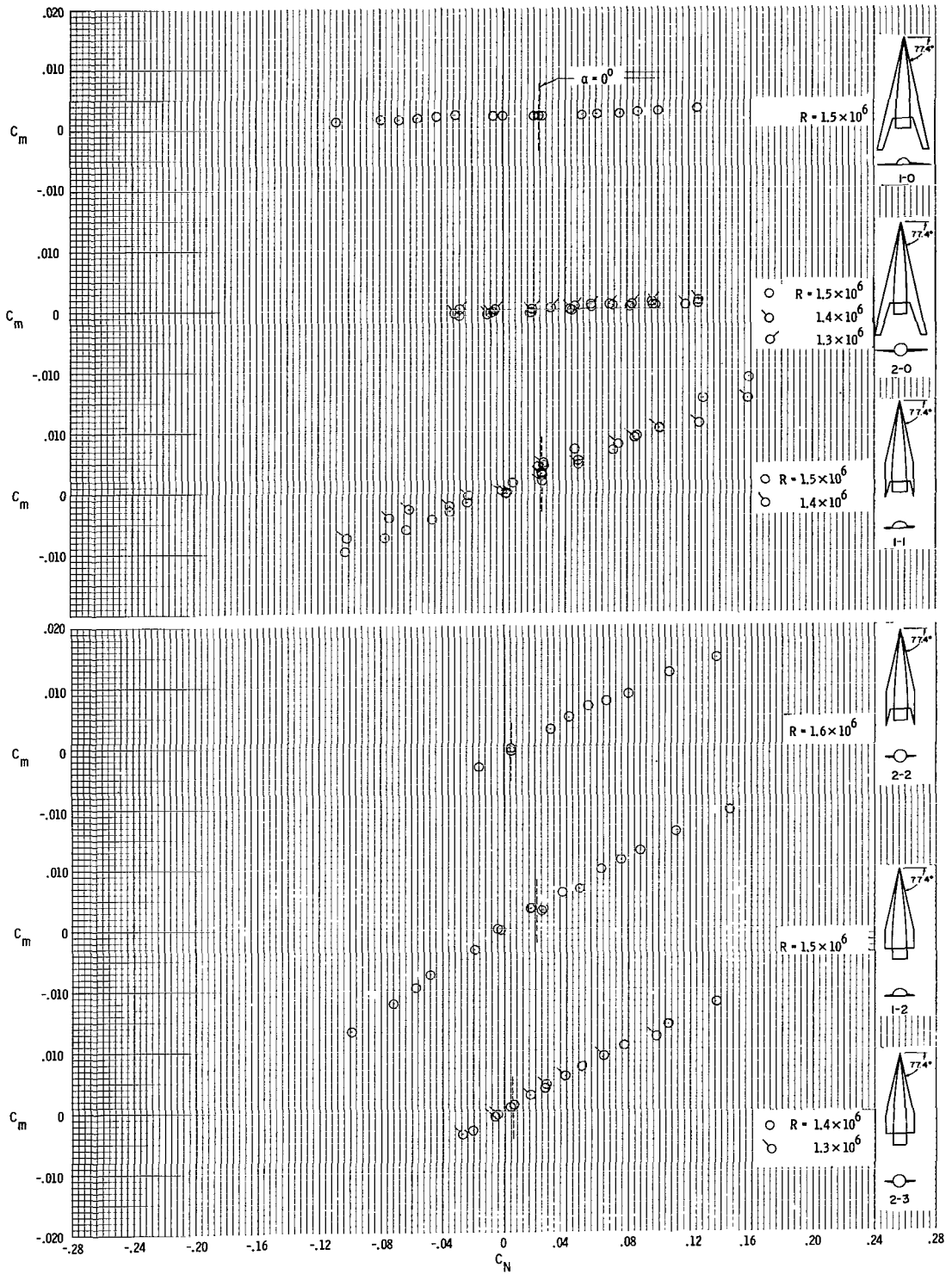
(a) Models 1-0, 2-0, 1-1, 2-2, 1-2, and 2-3.

Figure 15.- Pitching-moment coefficient as a function of normal-force coefficient at  $M = 9.6$ .



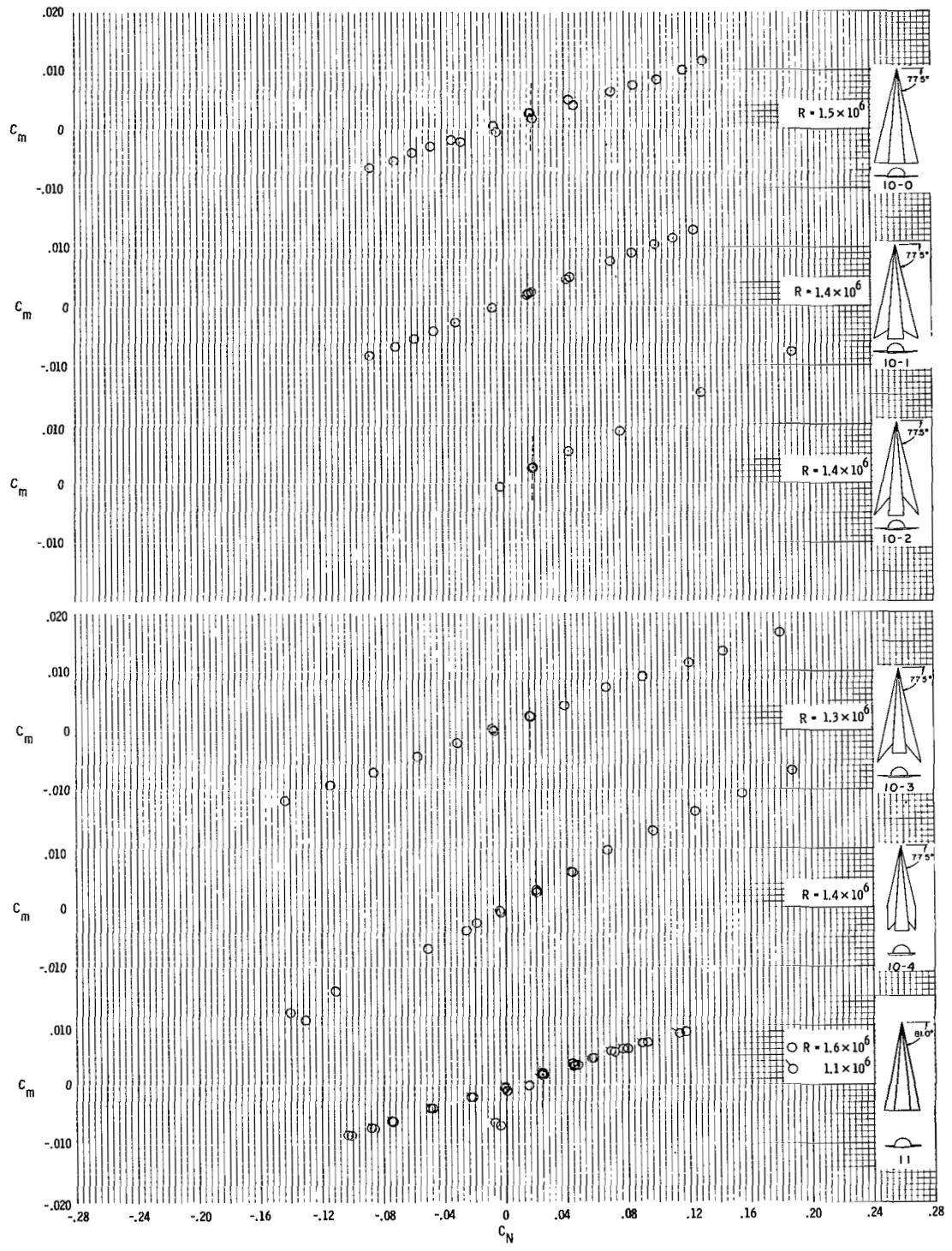
(b) Models 10-0, 10-4, 11, 13-0, 13-8, 13-9, and 9.

Figure 15.- Concluded.



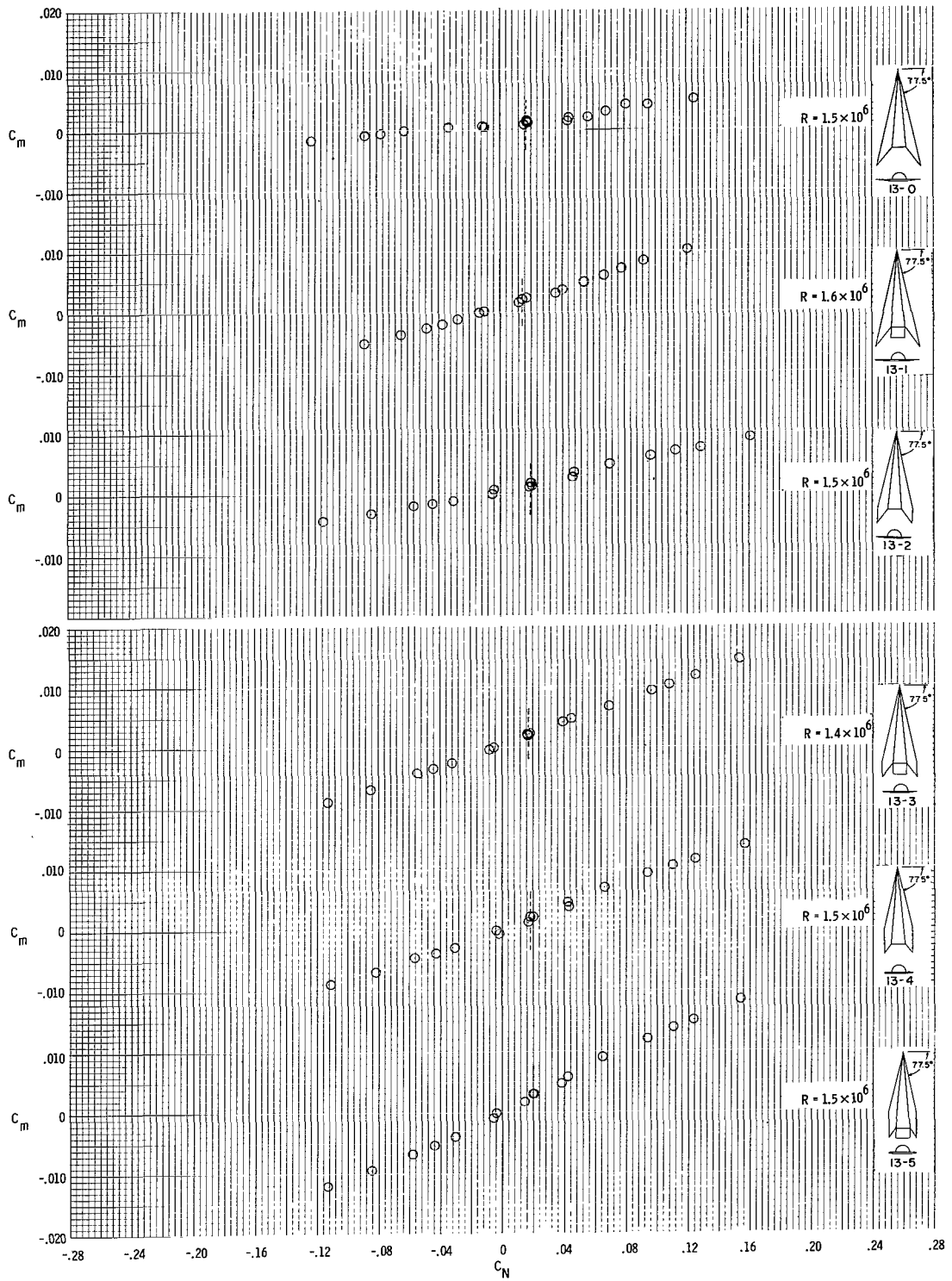
(a) Models 1-0, 2-0, 1-1, 2-2, 1-2, and 2-3.

Figure 16.- Pitching-moment coefficient as a function of normal-force coefficient at  $M = 6.8$ .



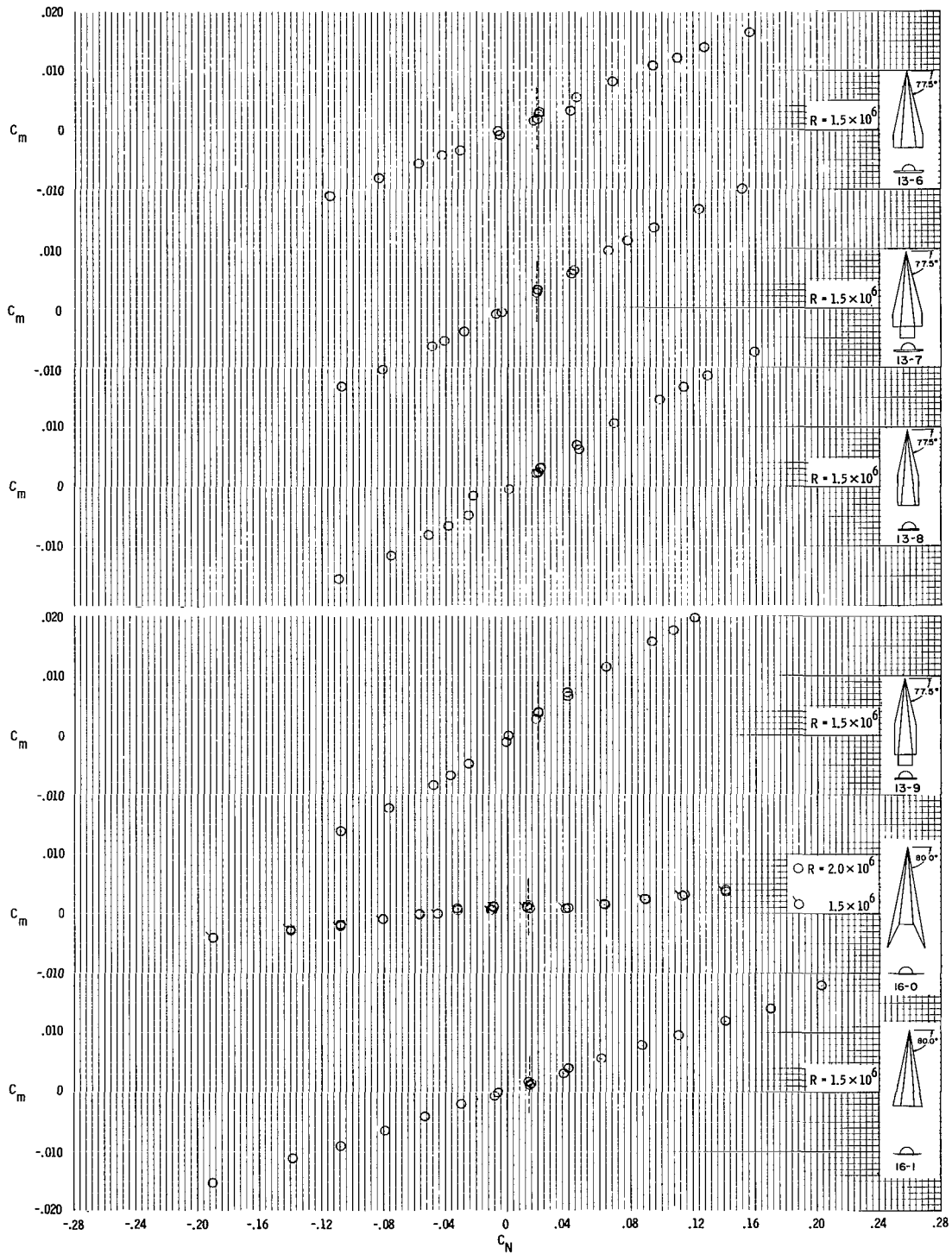
(b) Models 10-0, 10-1, 10-2, 10-3, 10-4, and 11.

Figure 16.- Continued.



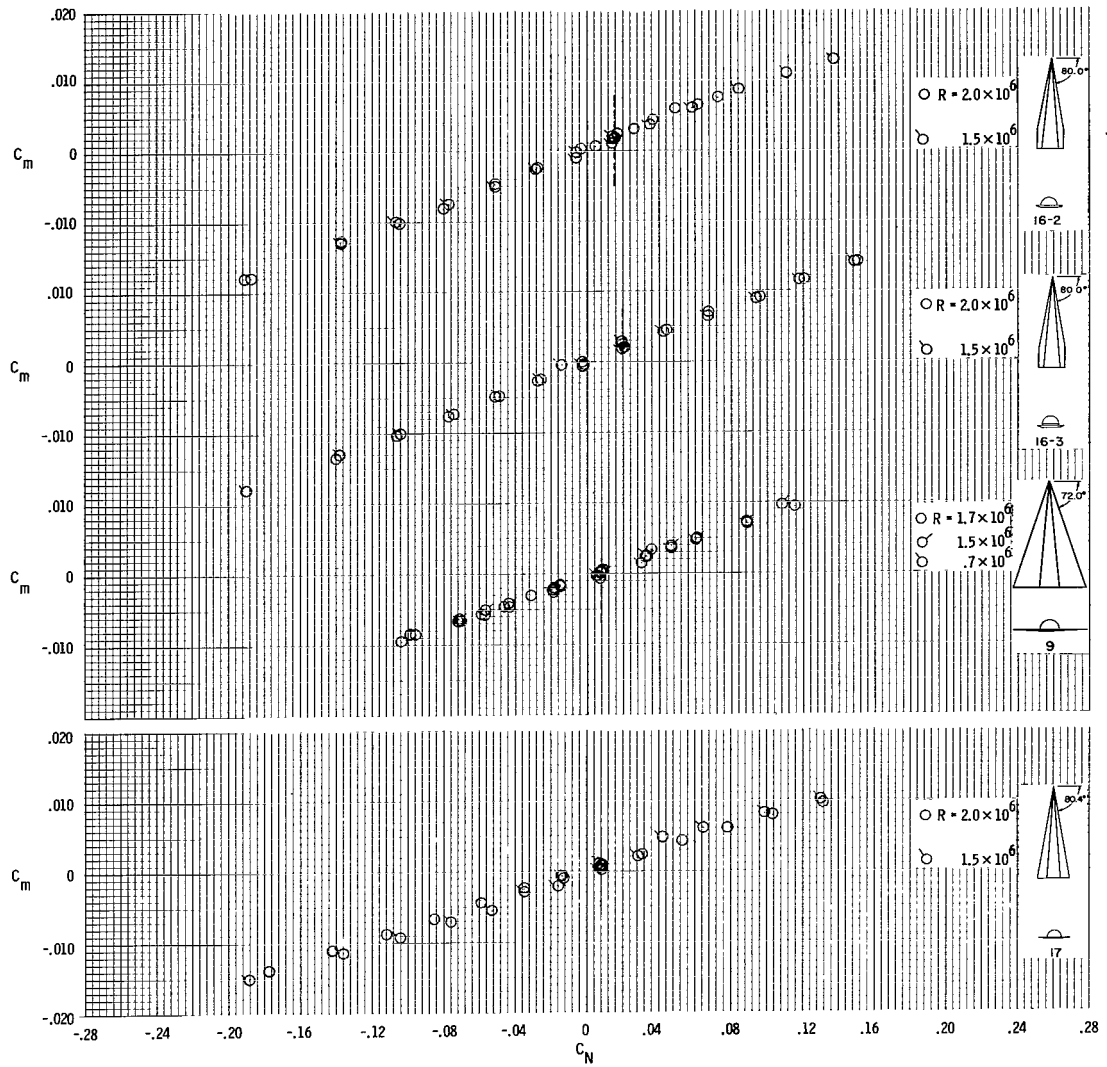
(c) Models 13-0, 13-1, 13-2, 13-3, 13-4, and 13-5.

Figure 16.- Continued.



(d) Models 13-6, 13-7, 13-8, 13-9, 16-0, and 16-1.

Figure 16.- Continued.



(e) Models 16-2, 16-3, 9, and 17.

Figure 16.- Concluded.

*"The aeronautical and space activities of the United States shall be conducted so as to contribute . . . to the expansion of human knowledge of phenomena in the atmosphere and space. The Administration shall provide for the widest practicable and appropriate dissemination of information concerning its activities and the results thereof."*

—NATIONAL AERONAUTICS AND SPACE ACT OF 1958

## NASA SCIENTIFIC AND TECHNICAL PUBLICATIONS

**TECHNICAL REPORTS:** Scientific and technical information considered important, complete, and a lasting contribution to existing knowledge.

**TECHNICAL NOTES:** Information less broad in scope but nevertheless of importance as a contribution to existing knowledge.

**TECHNICAL MEMORANDUMS:** Information receiving limited distribution because of preliminary data, security classification, or other reasons.

**CONTRACTOR REPORTS:** Technical information generated in connection with a NASA contract or grant and released under NASA auspices.

**TECHNICAL TRANSLATIONS:** Information published in a foreign language considered to merit NASA distribution in English.

**TECHNICAL REPRINTS:** Information derived from NASA activities and initially published in the form of journal articles.

**SPECIAL PUBLICATIONS:** Information derived from or of value to NASA activities but not necessarily reporting the results of individual NASA-programmed scientific efforts. Publications include conference proceedings, monographs, data compilations, handbooks, sourcebooks, and special bibliographies.

*Details on the availability of these publications may be obtained from:*

SCIENTIFIC AND TECHNICAL INFORMATION DIVISION  
NATIONAL AERONAUTICS AND SPACE ADMINISTRATION  
Washington, D.C. 20546